Dimensional crossover in ultracold Fermi gases from functional renormalization

Bruno M. Faigle-Cedzich [1], Jan M. Pawlowski [1,2] and Christof Wetterich [1]

[1]*Institute for Theoretical Physics, Heidelberg University, D-69120 Heidelberg, Germany*
[2]*ExtreMe Matter Institute (EMMI), GSI Helmholtzzentrum für Schwerionenforschung mbH, D-64291 Darmstadt, Germany*

We investigate the dimensional crossover from three to two dimensions in an ultracold Fermi gas across the whole BCS-BEC crossover. Of particular interest is the strongly interacting regime as strong correlations and pair fluctuations are more pronounced in reduced dimensions. Our results are obtained from first principles within the framework of the functional renormalization group (FRG). Here, the confinement of the transverse direction is imposed by means of periodic boundary conditions. We calculate the equation of state, the gap parameter at zero temperature, and the superfluid transition temperature across a wide range of transversal confinement length scales. Particular emphasis is put on the determination of the finite-temperature phase diagram for different confinement length scales. In the end, our results are compared with recent experimental observations and we discuss them in the context of other theoretical works.

I. INTRODUCTION

Lower dimensional systems are of particular interest both in condensed matter and statistical physics as they feature a pronounced influence of fluctuations. Furthermore, they are of experimental and technological importance with examples ranging from high-temperature superconductors over layered semiconductors to graphene. To disentangle the effects of the dimensionality from other many-body physics effects constitutes a key challenge in the study of systems of reduced dimensionality.

With the recent progress in trapping ultracold atomic gases in quasi-two-dimensional geometries [1,2], both zero- [3,4,23] and finite-temperature effects [3,5–8,11,40] have been measured. Here, strongly anisotropic trapping potentials on the one hand and one-dimensional optical lattices one the other hand allow for the experimental realization of quasi-two-dimensional quantum gases.

For example, the algebraic correlations associated with the Berezinskii-Kosterlitz-Thouless (BKT) phase transition in (quasi-)two-dimensional systems have been observed in bosonic [5,9–13] and fermionic systems [6,14]. In addition, (quasi-)two-dimensional systems exhibit the breaking of the scale invariance in the strongly interacting regime of the BCS-BEC crossover. Here, extensive progress both in theory [15–22] and experiment [23–25] has been achieved in recent years.

Because of an insufficient degree of anisotropy in the experimental setup, one may not be restricted to a particular dimension but find oneself in a dimensional crossover without a well-defined dimensionality. Apart from being an undesired effect for the investigation of pure two-dimensional systems, the crossover may also lead to new materials with physically interesting properties.

We concentrate here on ultracold Fermi gases. A comparable quasi-two-dimensional setup has been studied in

Refs. [26,27] in a mean-field approach, for a Fermi gas at unitarity and zero temperature in Ref. [28], using the Luttinger-Ward approach in two dimensions in Ref. [29], and using Quantum Monte Carlo (QMC) calculations in two dimensions in Ref. [30]. Furthermore, two-dimensional fermionic systems have been addressed in Refs. [31–38]. Fermi gases, typically a system of ^{6}Li or ^{40}K, constitute a rich physical system as their interatomic interactions may be altered via a Feshbach resonance. For a large negative value of the three-dimensional scattering length a_{3D}, the fermions form large spatially overlapping Cooper pairs below a critical temperature (BCS limit). On the other hand, for large positive scattering lengths, the fermions form tightly bound molecular dimers which condense into a Bose-Einstein condensate (BEC) at sufficiently low temperatures.

Apart from featuring the transition to the superfluid phase, the normal-state "pseudogap" behavior can also be studied within the BCS-BEC crossover. Here, the onset of superfluidity and pairing occurs at different temperatures; i.e., the density of states is partially gapped and the dispersion relation is BCS-like for a range of temperatures above the critical temperature. The system essentially retains some features of the broken superfluid phase also in the symmetric normal phase without exhibiting superfluidity. This pairing at high temperatures has been studied both experimentally, e.g., in Refs. [39,40], as well as theoretically, e.g., in Refs. [41–43].

Moreover, a BCS-BEC crossover can also be found in confined superconducting systems, where the crossover is induced by tuning the chemical potential to a band edge in multiband superconductors. The size-induced molecule-like pairing has been studied both theoretically [44–47] and experimentally [48]. Here, the confinement of superconducting materials (e.g., in the form of monolayer systems) result in shape resonances where an increased temperature, gap, as well as intrapair correlation length are present. The step in the

density of states gives rise to a change in the topology of the Fermi surface, a so-called Lifshitz transition, and is another factor in an increased critical transition temperature [49–54]. For a one- to two-dimensional crossover, see, e.g., Ref. [55].

The BCS-BEC crossover has been studied extensively in three dimensions using functional renormalization group (FRG) techniques [56–70]. Finite-size effects have been investigated in both cold-atom systems [28,71] and in quantum chromodynamics (QCD) [72–74].

In this work, we study the dimensional crossover from three to two spatial dimensions for ultracold Fermi gases by means of the functional renormalization group; for a study of nonrelativistic bosonic systems, see Ref. [75]. In particular, we are interested in the critical temperature for the superfluid transition over the BCS-BEC crossover in dependence of the dimensionality.

The dimensional crossover is achieved by compactifying the "transverse" z direction by a potential well of length L. We discuss (anti)periodic boundary conditions, as well as a confinement to a box with boundaries fixed to zero. The compactification leads to a discrete momentum spectrum in the z direction. The choice of the boundary conditions is crucial for a well-defined two-dimensional limit. It also influences the mapping between three- and two-dimensional parameters of the Fermi gas. Both aspects are discussed in detail in Sec. II C.

This paper is organized as follows: In Sec. II, we introduce the ultracold Fermi gas and the functional renormalization group (FRG) in the dimensional crossover. In particular, we discuss the aspect of boundary conditions for a dimensional reduction. The truncation used within the FRG and the initial conditions are presented in Sec. III. In Sec. IV, the results for the equation of state and the gap parameter in the dimensional crossover at zero temperature are discussed. The finite-temperature phase diagrams with respect to the dimensionality are addressed in Sec. V. We conclude in Sec. VI. Some technical details are deferred to Appendixes A–C.

II. MODEL AND FUNCTIONAL RENORMALIZATION

A. Model

Close to a broad Feshbach resonance, as found in quantum gases consisting of ^{6}Li and ^{40}K, details of the atomic interactions in ultracold Fermi gases become irrelevant for the description of the macrophysics. The system can then be described by a universal action

$$S[\psi] = \int_X \left[\sum_{\sigma=1,2} \psi_\sigma^*(\partial_\tau - \nabla^2 - \overline{\mu})\psi_\sigma + \overline{\lambda}_\psi \psi_1^* \psi_2^* \psi_2 \psi_1 \right],$$
(1)

where ψ_σ and ψ_σ^* denote Grassmann fermions in the hyperfine state $\sigma = 1, 2$. We introduce $X = (\tau, \vec{x})$ with τ being the Euclidean time and $\int_X = \int_0^\beta d\tau \int d^d x$ with spatial dimension d. Moreover, the chemical potential $\overline{\mu}$ and the four-Fermi coupling $\overline{\lambda}_\psi \to \lambda_\psi = 8\pi a_{3D}$ are related to the physical chemical potential and the scattering length through an appropriate vacuum renormalization.

We use $\hbar = k_B = 2M = 1$ with M being the mass of the fermionic atoms. For sufficiently low temperatures, the ultracold Fermi gas may develop many-body instabilities resulting

in the formation of a macroscopic anomalous self-energy Δ which is related to the nonvanishing expectation value $\langle \psi_1 \psi_2 \rangle$. This is signaled by a divergence of the frequency- and momentum-dependent four-Fermi vertex at lower momentum scales and causes the breaking of the global U(1) symmetry. In particular, in the strongly coupled regime, i.e., for a diverging three-dimensional s-wave scattering length a_{3D}, the quantitative determination of this phase transition is complicated by the frequency and momentum dependence of the vertex. In order to resolve this difficulty, a scale-dependent treatment in the path integral formulation is appropriate.

The starting point is the grand canonical partition function of the system

$$Z[\eta, \overline{\eta}] = \int \mathcal{D}\overline{\psi} \, \mathcal{D}\psi \, e^{-S[\psi, \overline{\psi}] - \overline{\eta}\psi + \overline{\psi}\eta}.$$
(2)

In order to exclude redundancies included in the grand canonical partition function, the effective action may be introduced as the Legendre transform of the Wigner functional $W[\eta, \overline{\eta}] = \ln Z[\eta, \overline{\eta}]$

$$\Gamma[\psi, \overline{\psi}] = \int_X (\overline{\psi}_X \eta_X + \overline{\eta}_X \psi_X) - W[\eta, \overline{\eta}].$$
(3)

B. Functional renormalization

The nonperturbative functional renormalization group (FRG) allows for a scale-dependent study of physical systems and theoretical models. It is a modern implementation of Wilson's RG and enables one to go beyond perturbative methods; i.e., it is also applicable in strongly correlated regimes. The FRG is based upon an exact functional flow equation of a coarse-grained effective action (or Gibb's free energy, in the language of statistical physics), which allows for including (thermal and quantum) fluctuations on all scales. It encompasses both Bogoliubov theory and the hydrodynamic approach of Popov and is inherently free of divergences [76]. Functional renormalization proceeds in the same spirit as other functional methods used for the problem of dimensional crossover, e.g., in Refs. [29,32–34,37]. It has the advantage that several effects can be included simultaneously, and all known limits are directly realized.

For the scale-dependent treatment, the integration is grouped in frequency and momentum shells according to

$$q_0^2 + (\vec{q}^{\,2} - \mu)^2 \simeq k^4$$
(4)

with external momentum scale k. The full grand canonical partition function is obtained by successively integrating over the corresponding frequency and momentum shells starting at $k = \infty$ and arriving in the end at $k = 0$.

The microscopic action in (1) is related to an ultraviolet (UV) momentum scale $k = \Lambda$ at length scales much smaller than the van der Waals length ℓ_{vdW}. However, the relevant physics takes place at scales $\ll \Lambda$, where the thermal and quantum fluctuations are included. To incorporate these fluctuations and furthermore to obtain results in the strongly coupled regime, the above scale-dependent procedure is implemented via the functional renormalization group (FRG), which includes these fluctuations successively at each momentum scale k. Introducing the scale-dependent partition

function

$$Z_k[\eta, \overline{\eta}] = \int \mathcal{D}\overline{\psi}\,\mathcal{D}\psi\, e^{-S[\psi] - \Delta S[\psi] - \overline{\eta}\psi + \overline{\psi}\eta}, \qquad (5)$$

we incorporate the suppression of the low-momentum fluctuations $\omega, \vec{q} \ll k^2$ via a masslike infrared modification of the dispersion relation. In practice, a regulator or cutoff term $\Delta S_k[\psi]$ is added to the microscopic action $S[\psi]$ being quadratic in the fields

$$\Delta S[\psi] = \int_Q \sum_{\sigma=1,2} \psi_\sigma(-Q)\, R_\psi(Q)\, \psi_\sigma(Q). \qquad (6)$$

The regulator $R_k(Q)$ may be chosen freely with the requirements

$$\lim_{q^2/k^2 \to 0} R_k(Q) = k^2, \qquad \lim_{q^2/k^2 \to \infty} R_k(Q) = 0. \qquad (7)$$

The scale-dependent effective action Γ_k can be defined accordingly. Starting at $\Gamma_\Lambda = S$, the full effective action is reached after the inclusion of all fluctuations where Γ_k smoothly interpolates between the microscopic action Γ_Λ and the full effective action $\Gamma_{k=0} = \Gamma$. Each infinitesimal change of the average effective action is described by a flow equation $\partial_k \Gamma_k$ depending on the correlation function of the theory and a way to suppress infrared modes with momenta smaller than k. In the end, fluctuations with large wavelengths are included. Since the functional renormalization group includes the fluctuations stepwise, there are no infrared divergences when approaching the inclusion of long wavelength modes. Analogous to defining the quantum theory by means of the classical action in the path integral formulation, the initial effective action Γ_Λ together with the flow equation (8) determines the full quantum theory.

The infinitesimal change of the effective action Γ_k with respect to the momentum scale k is governed by the flow equation [64,76–85]

$$\partial_k \Gamma_k = \frac{1}{2} \mathrm{STr}\big[\big(\Gamma_k^{(2)} + R_k\big)^{-1} \partial_k R_k\big], \qquad (8)$$

where $\Gamma_k^{(2)}$ is the second functional derivative of Γ_k with respect to the fields. As the flow equation (8) is an integrodifferential equation, its full solution is in most cases out of reach. One therefore relies on approximation schemes to the full effective action Γ_k which should incorporate the examined physics already at lower order of the approximation and reduce the number of flow equations to a manageable set of couplings. Furthermore, it is convenient to rewrite the four-Fermi interaction λ_ψ at a large cutoff Λ in terms of a bosonic degree of freedom ϕ via a Hubbard-Stratonovich transformation.

In this work, we choose a three-dimensional Litim-type regulator [86–88] for the cutoff function $R(Q)$ in three spatial dimensions. It is given for bosons and fermions, respectively, by

$$R_{\phi,k}(q^2) = (k^2 - q^2/2)\,\theta(k^2 - q^2/2),$$
$$R_{\psi,k}(q^2) = k^2\,(\mathrm{sgn}(z) - z)\,\theta(1 - |z|), \qquad (9)$$

where $\theta(x)$ represents the Heaviside-θ function, $\mathrm{sgn}(x)$ is the sign function, and we used $z = (q^2 - \mu)/k^2$. Note that only spatial momenta $q^2 = |\vec{q}|^2$ are regularized for this type of

regulator. However, a particular neat property of (9) is that the finite-temperature Matsubara sums can be performed analytically.

C. Function space and boundary conditions

The choice of the boundary conditions plays a crucial role in arriving at the correct two-dimensional physics. The dimensional crossover is implemented by compactifying the "transverse" z direction by a potential well of length L,

$$V_{\mathrm{box}}(z) = \begin{cases} 0 & 0 \leqslant z \leqslant L \\ \infty & \text{else} \end{cases}. \qquad (10)$$

One may choose (anti)periodic boundary conditions

$$\psi(x, y, z = 0) = \pm\psi(x, y, z = L), \qquad (11)$$

or restrict oneself to a box

$$\psi(x, y, z = 0) = \psi(x, y, z = L) = 0. \qquad (12)$$

The compactification leads to a discrete momentum spectrum in the z direction. For periodic boundary conditions, the respective energies, $E_z = \frac{\hbar q_z^2}{2M}$, are discrete with $q_z \to k_n$

$$k_n = \frac{2\pi n}{L}, \quad n \in \mathbb{Z}, \qquad (13)$$

which includes a zero mode $k_0 = 0$ with vanishing energy $E_{\min} = 0$. In turn, for antiperiodic boundary conditions, one finds $k_n = (2n+1)\pi/L$ with $n \in \mathbb{Z}$ and with a lowest mode $|k_0| = \pi/L$ with a finite energy $E_{\min} = \hbar\pi^2/(2ML^2)$. Finally, confining the Fermi gas inside a box leads to $k_n = \pi n/L$ with a vanishing energy $E_{\min} = 0$.

The nonvanishing zero point energy for antiperiodic boundary conditions results in a gap in the evaluation of the the (discrete) mode sum at zero temperature. Consequently, antiperiodic boundary conditions do not yield the two-dimensional limit for vanishing length $L \to 0$. For a relativistic system, the dispersion relations allows one to identify the length of the potential well L with the inverse temperature $1/T$ in the evaluation of the discrete mode sum at zero temperature. As a result, $T = 0$ and $L = L_0$ gives the same result as $T = 1/L_0$ and $L = 0$; i.e., the zero length limit $L \to 0$ at zero temperature $T = 0$ corresponds to the limit of infinite temperature $T \to \infty$ at zero length $L = 0$. For a nonrelativistic system, the situation is less simple, since the dispersion relation allows no clear mapping between the temperature and the length of the system. Nevertheless, it is clear that antiperiodic boundary conditions do not admit a two-dimensional limit for $L \to 0$.

Here we choose periodic boundary conditions, which result in a two-dimensional limit for vanishing length $L \to 0$. Since all modes with $n \neq 0$ have for $L \to 0$ a large gap, they can be integrated out. In general, the three-dimensional system with finite L can be viewed as a two-dimensional system with infinitely many fermions as "modes," one for each n. Integrating out the modes with $n \neq 0$ reduces the system to a single two-dimensional fermion, the one for $n = 0$.

The map from the three-dimensional system to the two-dimensional system proceeds by integrating out the $n \neq 0$ modes. This maps the parameters of the three-dimensional

theory to the ones of an effective two-dimensional theory. For $L \to 0$, this map may induce large changes for characteristic quantities as the chemical potential μ or the scattering length a. This can lead to shifts in fractions including ϵ_F and T_F, as well as in the crossover parameter. For experiment, the three-dimensional quantities are generally the ones available, and we will typically use them for our discussion. When comparing to results obtained from computations in two-dimensions, the matching between three- and two-dimensional parameters becomes important, however. In the present paper, we do not deal with this issue, but the reader should keep it in mind when comparing with two-dimensional results.

Experimentally realistic confinement potentials, used in most ultracold atom experiments, such as in Refs. [6,7] are implemented by using harmonic trapping potentials. Here, the function space consists of Hermite polynomials. Heuristically, our choice is a limiting case. In particular, observables that do not show an impact of the different boundary conditions studied here should be the same for the harmonic trap.

D. Dimensional reduction

In order to obtain a system within the dimensional crossover from three to two dimensions, we initialize the renormalization group (RG) flow at ultraviolet cutoff scale $k = \Lambda$ where the effective action Γ_Λ coincides with the microscopic action of a three-dimensional ultracold Fermi gas. By delimiting the z direction of the system via a potential well of length L, we introduce an additional scale to the three-dimensional system. By following the RG as a function of k for a given length scale L, one observes that the contribution of modes with $k_n^2 \gg k^2$ is suppressed by powers of k^2/k_n^2. These modes decouple and effective dimensional reduction is achieved automatically once $k \ll 2\pi/L$. This is very similar to the effective dimensional reduction in finite-temperature quantum field theory realized by solutions of the flow equations [89]. Following the RG from $k = \Lambda$ to $k = 0$, the flow always makes a transition from a three-dimensional regime to a two-dimensional one. For this purpose, the UV scale is always chosen such that $\Lambda \gg (L^{-1}, \mu^{1/2}, T^{1/2})$. The flow equations become effectively two-dimensional for $k \ll 2\pi/L$, while the physical system is effectively two-dimensional if L^{-1} is much larger than all other many-body scales [75].

To incorporate the effects of the compactification in transversal z direction given by the potential well in (10), the regulators in (9) are modified according to

$$\vec{q}^2 = \hat{q}^2 + q_z^2 \to \hat{q}^2 + k_n^2, \tag{14}$$

where k_n is chosen according to the boundary conditions and $\hat{q}^2$ denotes the square of the x and y components of the momentum. Note that while in three dimensions all couplings tend to saturate quickly at sufficiently small k scales [67], the saturation behavior is much slower for $d < 3$. As a consequence, we choose a much smaller final k scale in the infrared (cf. Appendix A), while in three dimensions it is possible to stop the RG flow earlier.

III. RUNNING OF COUPLINGS

A. Truncation

After a Hubbard-Stratonovich transformation, the full microscopic action is given by

$$S = \int_X \left[\sum_{\sigma=1,2} \psi_\sigma^* (\partial_\tau - \nabla^2 - \overline{\mu}) \psi_\sigma \right.$$
$$\left. + m_\phi^2 \, \phi^* \phi - h \, (\phi^* \, \psi_1 \, \psi_2 - \phi \, \psi_1^* \, \psi_2^*) \right], \tag{15}$$

with $\overline{\lambda}_\psi = -h^2/m_\phi^2$, which can be seen via a Gaussian integration over the bosonic field ϕ. The Feshbach coupling h accounts for the interconversion of two fermionic atoms ψ with different spin to a bosonic dimer ϕ. Connecting the above action to the experimental setup, we explicitly introduce the closed channel via the bosonic field ϕ. The physical detuning $\nu = \nu(B)$, which depends on the external magnetic field of the trap in the experiment, denotes the distance of the closed-channel bound state from the scattering threshold. In the kinetic term of the bosonic dimer ϕ, the factor of $\nabla^2/2$ reflects the composite mass of the dimer, while this composition also yields twice the chemical potential for the bosons

$$S[\psi, \phi] = \int_X \left[\psi^* (\partial_\tau - \nabla^2 - \mu) \psi \right.$$
$$+ \phi^* \left(\partial_\tau - \frac{\nabla^2}{2} + \nu - 2\mu \right) \phi$$
$$\left. - h \, (\phi^* \, \psi_1 \, \psi_2 - \phi \, \psi_1^* \, \psi_2^*) \right]. \tag{16}$$

Our ansatz for the effective average action can be divided into a kinetic part and an interaction part

$$\Gamma_k = \Gamma_{\text{kin}} + \Gamma_{\text{int}}. \tag{17}$$

The kinetic part describes the fermion and boson dynamics and is given by

$$\Gamma_{\text{kin}} = \int_X \left[\sum_{\sigma=\{1,2\}} \overline{\psi}_\sigma^* \, \overline{P}_{\psi,\sigma}(Q) \, \overline{\psi}_\sigma + \overline{\phi}^* \, \overline{P}_\phi(Q) \, \overline{\phi} \right], \tag{18}$$

with unrenormalized (unrescaled) fields $\overline{\psi}$, $\overline{\phi}$ and inverse propagators

$$\overline{P}_{\psi\sigma}(Q) = Z_{\psi\sigma} \, i \, q_0 + A_{\psi\sigma} \, q^2 - \overline{\mu},$$
$$\overline{P}_\phi(Q) = Z_\phi \, i \, q_0 + A_\phi \, q^2/2. \tag{19}$$

In terms of the renormalized (rescaled) fields $\psi = A_\psi^{1/2} \, \overline{\psi}$ and $\phi = A_\phi^{1/2} \, \overline{\phi}$, the kinetic part can be formulated as

$$\Gamma_{\text{kin}}[\psi, \phi] = \int_X \left[\sum_{\sigma=\{1,2\}} \psi_\sigma^* (S_\psi \, \partial_\tau - \nabla^2 - \mu) \, \psi_\sigma \right.$$
$$\left. + \phi^* \left(S_\phi \, \partial_\tau - \frac{1}{2} \nabla^2 \right) \phi \right]. \tag{20}$$

We normalized the coefficients of the gradient terms by means of the wave function renormalizations A_ψ and A_ϕ which enter
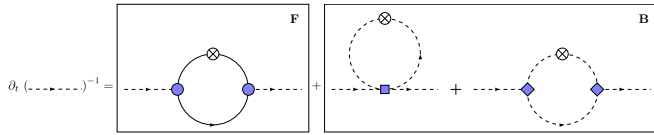
FIG. 1. (F) and (B) truncation schemes of the flow equations. The flow of the inverse boson propagator incorporates both fermionic and bosonic diagrams. Bosonic propagators correspond to dashed and fermionic propagators to solid lines, while the distinct vertices are shown in different shapes. The regulator insertion is denoted by a cross.

the renormalization group flow via the anomalous dimensions

$$\eta_\psi = -\partial_t \ln A_\psi, \quad \eta_\phi = -\partial_t \ln A_\phi. \quad (21)$$

Moreover, we defined $S_{\psi,\phi} = Z_{\psi,\phi}/A_{\psi,\phi}$ and the renormalized chemical potential $\mu = \bar\mu/A_{\psi,\sigma}$. For a more detailed description, we refer to Appendix C.

Due to the renormalization of the fields, the expectation value $\Delta = (h^2 \rho)^{1/2}$ can be nonzero, even in the two-dimensional limit [75], where the Mermin-Wagner theorem [90,91] forbids true long-range order. However, algebraically decaying correlation functions with a nonvanishing superfluid density can be found [92–95].

The interactions can, after the Hubbard-Stratonovich transformation, be written as

$$\Gamma_{\rm int}[\psi, \phi] = \int_X [U(\phi^* \phi) - h (\phi^* \psi_1 \psi_2 - \phi \psi_1^* \psi_2^*)]. \quad (22)$$

The effective average potential $U(\rho)$ depends only on the $U(1)$-invariant quantity $\rho = \phi^* \phi$ and describes bosonic scattering processes. The $U(1)$ symmetry is spontaneously broken for a nonzero minimum ρ_0 of the effective average potential and thus describes superfluidity. In a Taylor expansion, we write

$$U(\rho) = m_\phi^2 (\rho - \rho_0) + \frac{\lambda_\phi}{2}(\rho - \rho_0)^2 + \sum_{n=3}^N \frac{u_n}{n!}(\rho - \rho_0)^n, \quad (23)$$

where we need to include at least up to the second order in ρ to reproduce the second-order phase transition to superfluidity. In the symmetric regime, we therefore have $\rho_0 = 0$ and positive bosonic mass $m_\phi^2 > 0$, whereas the symmetry-broken regime is realized for $\rho_0 > 0$ and vanishing bosonic mass $m_\phi^2 = 0$. In the following, we restrict this work to order ϕ^4.

The truncation can be classified by the diagrams in Fig. 1 included on the right-hand side of the flow equation (8). By including only fermionic diagrams (F), we arrive at the mean-field result. Bosonic fluctuations enter the flow equation by including diagrams with two internal bosonic lines (B).

Furthermore, the flow of the density of the Fermi gas is calculated via a derivative of the effective action with respect to the chemical potential

$$\partial_k n_k = -\partial_k \frac{\partial U(\rho)}{\partial \mu}. \quad (24)$$

In practice, we approximate the dependence of the effective average action on the chemical potential by an expansion in ρ

and μ [63]

$$U(\rho) = \sum_{n=1}^2 \frac{u_n}{n!}(\rho - \rho_0)^n - n_k \, \delta\mu + \alpha_k \, (\rho - \rho_0)\, \delta\mu. \quad (25)$$

Here the chemical potential is split into a reference part μ_0 and an offset $\delta\mu$, such that $\mu = \mu_0 + \delta\mu$.

B. Initial conditions and universality

In three dimensions, the running couplings approach fixed points in the renormalization group flow of the Fermi gas. As a result, the macrophysics (on the length scales of the interparticle spacing) becomes independent of the microphysics (on the molecular scales) to a large extent; cf., e.g., Refs. [63,67].

When reaching the fixed points, the system loses its memory of the microphysics with its initial conditions. Consequently, the initial conditions of the running couplings are irrelevant and we may essentially start at the fixed point values in the ultraviolet. Even if we had not done so, they would be immediately generated.

An exception constitutes the bosonic mass term m_ϕ^2 whose fixed point is unstable toward the infrared. Hence, for the effective potential we set as initial condition in the ultraviolet

$$U_\Lambda(\rho) = (\nu_\Lambda - 2\,\mu)\,\rho. \quad (26)$$

Herein the chemical potential μ can be artificially split into a vacuum component $\mu_{\rm v}$ and a many-body contribution $\mu_{\rm mb}$ such that the vacuum part $\mu_{\rm v}$ equals half the binding energy of a bosonic dimer $\epsilon_B/2$ in three spatial dimensions. The detuning ν_Λ is related to the physical detuning via an appropriate vacuum renormalization [63].

Since the RG flow for a system in reduced dimension is initialized at an UV scale where the Fermi gas is described by the three-dimensional classical action, these considerations can be applied to the study of systems inside the dimensional crossover. We therefore choose the fixed point values of the three-dimensional Fermi gas as our initial conditions.

IV. DIMENSIONAL CROSSOVER AT ZERO TEMPERATURE

The flow equations underlying the results at zero and at finite temperature shown below are obtained analytically with periodic boundary conditions for both bosonic and fermionic fields inside the potential well. They are given in Appendix C. Imposing antiperiodic boundary conditions for fermionic fields $\psi(x)$ we find, as expected in Sec. II C, that for small confinement length scales $L\sqrt{\mu_{\rm mb}} \approx 2$ the fermionic flow is strongly suppressed and no phase transition on the BCS side of the crossover can be found. The BEC side, however, is not affected by this choice.

As described in Sec. II D, all running couplings saturate quickly in the infrared for the three-dimensional BCS-BEC crossover, while we for $d < 3$ chose for all observables a final scale of $t_{\rm final} = -17$ in the infrared. It is chosen such that for a small (quasi-)two-dimensional system of confinement length of $L\sqrt{\mu_{\rm mb}} = 0.7$ the maximum temperature for the BCS-BEC crossover converges; cf. Appendix A for a more detailed comparison on the final IR scale of the RG flow.
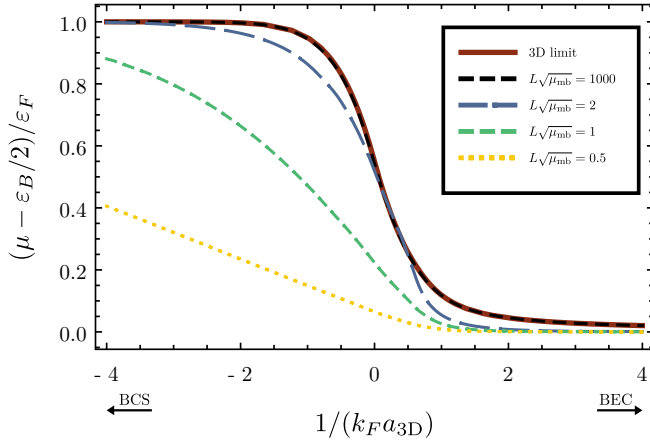
FIG. 2. Comparison of the equation of state at zero temperature for different confinement length scales and the three-dimensional case with respect to the 3D crossover parameter $1/(k_F \, a_{3D})$ for $t_{\text{final}} = -17$. From top to bottom: 3D limit in solid red (solid gray), $L \sqrt{\mu_{\text{mb}}} = 1000$ in dashed black, $L \sqrt{\mu_{\text{mb}}} = 2$ in long-dashed blue (long-dashed line in dark gray), $L \sqrt{\mu_{\text{mb}}} = 1$ in dashed green (dashed line in grey), $L \sqrt{\mu_{\text{mb}}} = 0.5$ in dotted yellow (dotted line in light gray). The three-dimensional case is recovered for large $L \sqrt{\mu_{\text{mb}}}$.

In order to display the confinement in transversal direction, we introduce the dimensionless length parameter $L \sqrt{\mu_{\text{mb}}}$ of the potential well, where $\mu_{\text{mb}} = \mu - \epsilon_B/2$ denotes the chemical potential for the three-dimensional gas with half the dimer binding energy $\epsilon_B/2$ being subtracted.

At zero temperature, a reduction of the dimensionless confinement length parameter $L \sqrt{\mu_{\text{mb}}}$ leads to an increased density and thereby to an increased Fermi energy $\epsilon_F = k_F^2$. As a consequence, the equation of state $(\mu - \epsilon_B/2)/\epsilon_F$ in Figs. 2 and 3 is lowered for more confined systems.

Here the Fermi momentum is calculated using the three-dimensional definition $k_F = (3 \pi^2 n)^{1/3}$ as the initial condition for the flow of the density is explicitly given for a three-dimensional system. This means that the Fermi momentum k_F of the (quasi-)two-dimensional system has to be calculated by using the functional form given in the ultraviolet, where the reduced dimension enters via the flow of the density.

In Fig. 2, the equation of state is shown as a function of the three-dimensional crossover parameter $c^{-1} = (k_F \, a_{3D})^{-1}$, which can be interpreted as the inverse concentration of the Fermi gas. For large confinement length scales $L \sqrt{\mu_{\text{mb}}}$, the three-dimensional result is recovered, while the equation of state in dependence of the transversal extension starts to saturate only at the order of $L \sqrt{\mu_{\text{mb}}} = 10^{-4}$ for a two-dimensional limit.

For better comparison to experiment, the equation of state is also displayed in Fig. 3 with respect to the two-dimensional crossover parameter $\ln(k_F \, a_{2D})$. Here the (quasi-)two-dimensional scattering length a_{2D} is calculated by [75]

$$a_{2D}^{(\text{pbc})} = L \exp\left\{ -\frac{1}{2} \frac{L}{a_{3D}} \right\} \tag{27}$$
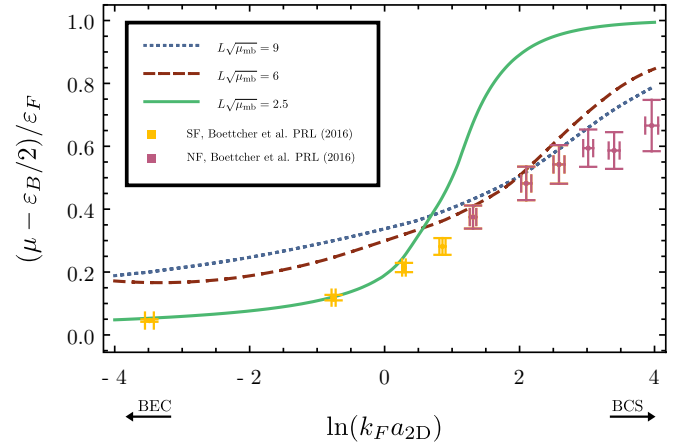

FIG. 3. Comparison of the equation of state for different confinement length scales to the experimental data from [3] with respect to the 2D crossover parameter $\ln(k_F \, a_{2D})$ for $t_{\text{final}} = -17$. Here we show $L \sqrt{\mu_{\text{mb}}} = 9$ in dotted blue (dotted line in gray), $L \sqrt{\mu_{\text{mb}}} = 6$ in dashed red (dashed line in dark gray), and $L \sqrt{\mu_{\text{mb}}} = 2.5$ in solid green (solid line in light gray). The experimental data are obtained for the lowest attainable temperatures of $T/T_F \approx 0.05$ on the BEC side and $T/T_F \approx 0.1$ on the BCS side. The orange and purple (light gray and dark gray) squares denote measurements in the superfluid and normal phase.

for our setup with periodic boundary conditions. Comparing the result in Fig. 2 with the experimental data found in Ref. [3] for a (quasi-)two-dimensional setup, we find a qualitatively good agreement. Especially on the BEC side, where the measurements were obtained in the superfluid phase, the equation of state for lower values of the confinement length $L \sqrt{\mu_{\text{mb}}}$ in our result yields the correct behavior. However, on the BCS side, the equation of state for confinements $L \sqrt{\mu_{\text{mb}}} \lesssim 6$ does not give the quantitative correct result. This behavior might be on the one hand attributed to an insufficient precision in the determination of the density. For a more elaborate way to obtain the density, see Appendix B. On the other hand, as mentioned in Sec. II C, the two-dimensional limit for periodic boundary conditions may feature parameters which do not coincide with the ones in three dimensions.

Comparing the gap parameter $\Delta = (h^2 \rho_0)^{1/2}$ with respect to the Fermi energy ϵ_F in Fig. 4 for different confinement length scales, one finds a flattening of the curve for lower dimensionality, while the three-dimensional case is recovered for large length scales $L \sqrt{\mu_{\text{mb}}}$. Interestingly, the gap saturates much more quickly for small length scales, already around $L \sqrt{\mu_{\text{mb}}} \simeq 0.5$ for a two-dimensional limit. Moreover, depending on the (three-dimensional) scattering length a_{3D}, regions of an increased gap Δ/ϵ_F can be found at intermediate length scales within the dimensional crossover. This diplike structure is a characteristic of the modes given by the boundary conditions chosen and is also found at finite temperature.

V. SUPERFLUID TRANSITION

A. Dimensional crossover of the critical temperature

At finite temperature, we study the behavior of the critical temperature T_c/T_F with respect to the spatial extension
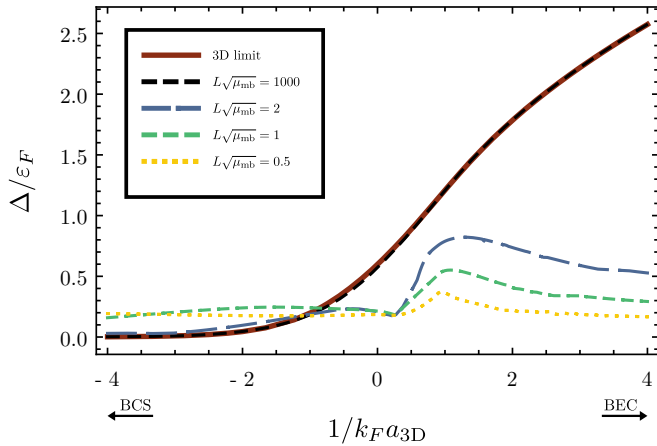
FIG. 4. Comparison of the gap parameter for different confinement length scales and the three-dimensional case with respect to the 3D crossover parameter $1/(k_F\, a_{3D})$ for $t_{final} = -17$. From top to bottom (on BEC side): 3D limit in solid red (solid line in gray), $L\sqrt{\mu_{mb}} = 1000$ in dashed black, $L\sqrt{\mu_{mb}} = 2$ in long-dashed blue (long-dashed line in dark gray), $L\sqrt{\mu_{mb}} = 1$ in dashed green (dashed line in gray), and $L\sqrt{\mu_{mb}} = 0.5$ in dotted yellow (dotted line in light gray). The three-dimensional case is recovered for large $L\sqrt{\mu_{mb}}$.

in transversal z direction $L\sqrt{\mu_{mb}}$. The Fermi temperature $T_F = k_F{}^2$ is, as in the zero temperature case, calculated using the three-dimensional relation between the Fermi momentum and the density $k_F = (3\pi^2 n)^{1/3}$. The order parameter for the superfluid transition is the (finite-temperature) gap $\Delta = (h^2\rho)^{1/2}$ in the fermion spectrum. The critical temperature is calculated as the largest temperature at which the gap Δ is nonvanishing. For a detailed description, see Appendix D.

For example, as shown for $a_{3D}^{-1} = 0$ in Fig. 5, one can identify a dimensional crossover from three to two dimensions for all values of the three-dimensional scattering length. The limiting case of three dimensions is reached for large confinement scales $L\sqrt{\mu_{mb}}$. Moreover, a distinct two-dimensional limit is obtained where the critical temperature in units of the Fermi temperature saturates and is significantly reduced with respect to the three-dimensional case. Note that as in the zero-temperature case IV we choose $t_{final} = -17$ for the final RG-flow scale.

Furthermore, one can clearly discern dips in the dimensional crossover of the critical temperature where we find an increased T_c/T_F at intermediate stages between the two- and three-dimensional limit. Interestingly, their appearance and amplitude seem to be related to the scattering length a_{3D} chosen in the ultraviolet. Moreover, we find a larger amplitude for more confined systems. This behavior is caused by the mode structure of a confined system specified by the chosen boundary conditions. As a consequence, the density of states for a confined system has a steplike structure and the dips can be found at the positions of the discontinuities. The dip structure for the critical temperature T_c/T_F emerge at the same confinement length scales $L\sqrt{\mu_{mb}}$ as for the zero-temperature gap parameter Δ. In a mean-field analysis with a confinement in transversal z direction induced by a harmonic potential on the weakly interacting BCS side of the BCS-BEC crossover, a similar diplike structure of the critical temperature was found
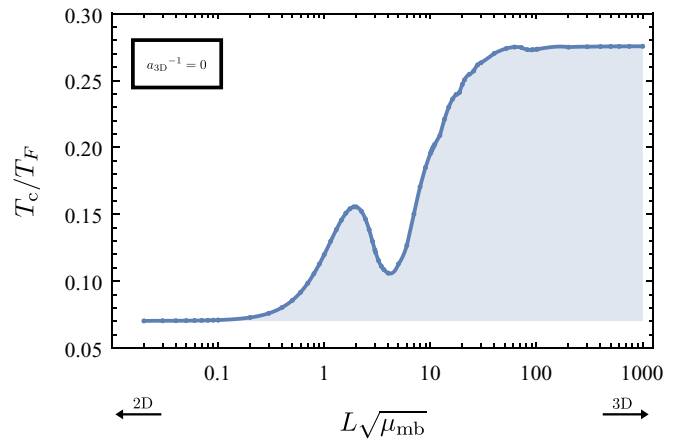

FIG. 5. Critical temperature T_c/T_F as a function of the confinement length scale $L\sqrt{\mu_{mb}}$ at an exemplary three-dimensional fermion scattering length of $a_{3D}^{-1} = 0$ for $t_{final} = -17$. Similar plots can be found for different scattering lengths with the difference being the amplitude and the position of the dips. These result from the mode structure caused by the chosen boundary conditions and are related to the steplike structure of the density of states for a confined system. Similar dips were also found in a mean-field analysis with a harmonic confinement [27].

[27]. The same behavior is seen in confined superconductors or thin superconducting films where the critical temperature, the gap parameter, and the intrapair correlation lengths are increased at so-called shape resonances [49–55].

B. Finite-temperature phase diagram

In Figs. 6 and 7, the critical temperature T_c/T_F as a function of the three-dimensional inverse concentration $c^{-1} =$
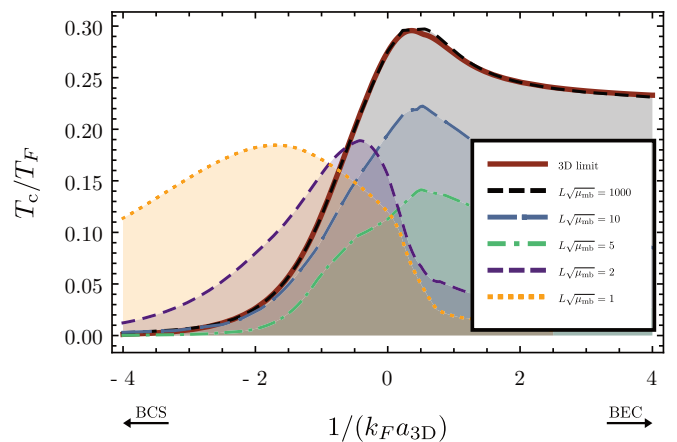

FIG. 6. Phase diagram in terms of T_c/T_F for different confinement length scales and the three-dimensional case with respect to the 3D crossover parameter $1/(k_F\, a_{3D})$ for $t_{final} = -17$. From top to bottom (on BEC side): 3D limit in solid red (solid line in gray), $L\sqrt{\mu_{mb}} = 1000$ in dashed black, $L\sqrt{\mu_{mb}} = 10$ in long-dashed blue (long-dashed line in gray), $L\sqrt{\mu_{mb}} = 5$ in dash-dotted green (dash-dotted line in lighter gray), $L\sqrt{\mu_{mb}} = 2$ in dashed purple (dashed line in dark gray), and $L\sqrt{\mu_{mb}} = 1$ in dotted orange (dotted line in light gray).
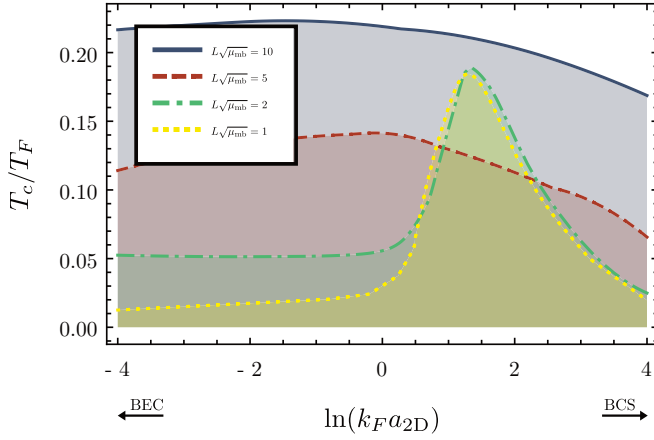
FIG. 7. Phase diagram in terms of T_c/T_F for different confinement length scales with respect to the 2D crossover parameter $\ln(k_F a_{2D})$ for $t_{final} = -17$. From top to bottom (on BEC side): $L \sqrt{\mu_{mb}} = 10$ in solid blue (solid line in dark gray), $L \sqrt{\mu_{mb}} = 5$ in dashed red (dashed line in gray), $L \sqrt{\mu_{mb}} = 2$ in dash-dotted green (dash-dotted line in lighter gray), and $L \sqrt{\mu_{mb}} = 1$ in dotted yellow (dotted line in light gray). The low critical temperature on the BEC side is caused by our choice of boundary conditions; see Sec. II C.

FIG. 8. Phase diagram in terms of T_c/T_F for a confinement length of $L \sqrt{\mu_{mb}} = 3.1$ with respect to $\ln(k_F a_{2D})$ for $t_{final} = -17$. Here we show the experimental data from Ref. [6] with the corresponding statistical errors in orange (light gray), as well as both the perturbative BKT- and BCS-transition temperatures as dashed red (dashed gray) lines in the appropriate regimes, i.e., $\ln(k_F a_{2D}) \ll -1$ (BEC) and $\ln(k_F a_{2D}) \gg 1$ (BCS).

$(k_F a_{3D})^{-1}$ and the two-dimensional crossover parameter $\ln(k_F a_{2D})$ is shown for different confinement length scales over the whole BCS-BEC crossover. The phase diagram in Fig. 6 approaches the three-dimensional limit for large confinement length scales, while the critical temperature is reduced for lower dimensionality over the BCS-BEC crossover. On the other hand, we find an increased critical temperature on the BCS side of the crossover around $L \sqrt{\mu_{mb}} = (0.5\ldots5)$. On the BEC side T_c/T_F continues to be reduced for more confined systems.

In Figs. 7 and 8, we find the expected exponential decrease on the BCS side of the crossover, where $\ln(k_F a_{2D}) \gg 1$, for small confinement scales in a quasi-two-dimensional geometry. Here it was found [96] that

$$\frac{T_c}{T_F} = \frac{2\,e^\gamma}{\pi\,k_F\,a_{2D}} \quad (28)$$

with the Euler number $\gamma \simeq 0.5772$. The critical temperature is lowered by a factor of e when including the Gorkov–Melik-Barkhudarov contribution [97,98].

Furthermore, the BKT-transition temperature on the BEC side, where $\ln(k_F a_{2D}) \ll 1$, is approximately reached for these length scales. However, for smaller $L \sqrt{\mu_{mb}}$, we obtain a smaller value than the predicted BKT transition temperature [98,99]

$$\frac{T_c}{T_F} = \frac{1}{2}\left\{\ln\left[\frac{\mathcal{B}}{4\,\pi}\,\ln\left(\frac{4\,\pi}{k_F^2\,a_{2D}^2}\right)\right]\right\}^{-1}, \quad (29)$$

with $\mathcal{B} \simeq 380$.

As described in Sec. II C, this behavior might be attributed to our choice of boundary conditions. Although we are arriving at a two-dimensional system using periodic boundary conditions, integrating out the higher modes in the transversal z direction may lead to a shift in the parameters of the Fermi gas. This shift can also be differently pronounced depending
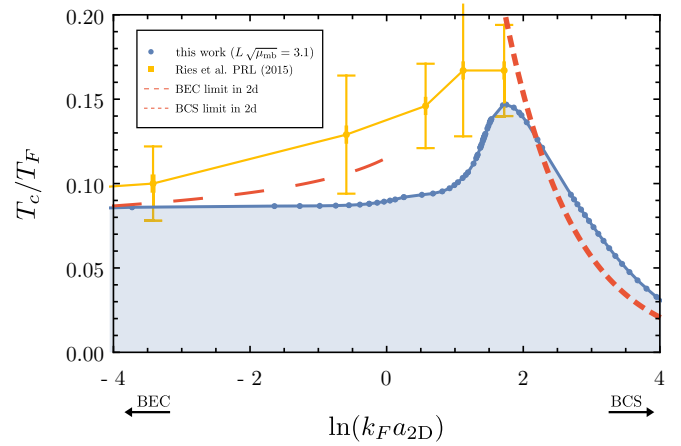
on the scattering length. The observation that T_c/T_F decreases toward zero on the BEC side for $L \to 0$ may be an indication for a strong L dependence in the map from three-dimensional to two-dimensional parameters in this region of the phase diagram and range of L.

In the region of strong correlations, where $\ln(k_F a_{2D}) \simeq 1$, we find a substantial increase in the critical temperature T_c/T_F which cannot be found in a mean-field analysis by extrapolation of the known BCS and BEC limits.

Comparing our results for $L \sqrt{\mu_{mb}} = 3.1$ to the experimental data from Ref. [6] in Fig. 8, where $L \sqrt{\mu_{mb}}$ is approximately of the order $0.5\ldots5$, we find a qualitatively similar phase diagram. Here the increased critical temperature in the strong coupling regime can also be found, yet slightly less pronounced.

In Fig. 9, we show our result for a confinement length of $L \sqrt{\mu_{mb}} = 3.1$ and the experimental data on the nonthermal fraction found in Ref. [6]. Here the preferred onset of a presuperfluid phase in the strongly correlated region is on par with our result of an increased superfluid temperature. The shift with respect to the two-dimensional crossover parameter can be assigned to the change in the parameters from three to two dimensions of the Fermi gas.

VI. CONCLUSIONS AND OUTLOOK

In this paper, we have studied the dimensional crossover in an ultracold Fermi gas from three to two dimensions, thus extending the work on nonrelativistic bosons carried out in Ref. [75] and the mean-field analysis in Ref. [27] for fermions. Particular emphasis was put on the superfluid phase transition calculated over the whole BCS-BEC crossover in dependence on different confinement length scales. A comparison to recent experiments in Refs. [3,6] found a qualitative good agreement. Moreover, we find a nontrivial behavior of the finite-temperature phase diagram when confining the Fermi
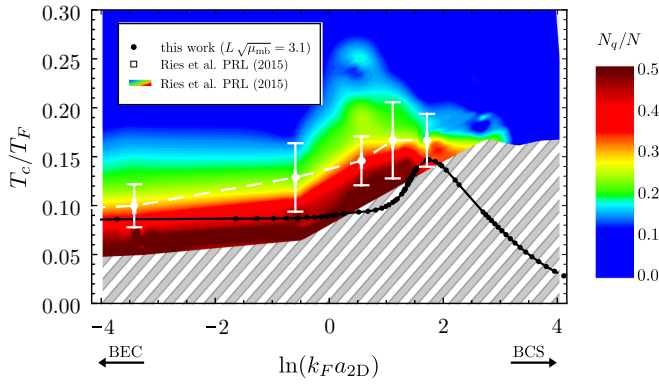
FIG. 9. Phase diagram in terms of T_c/T_F for a confinement length of $L\sqrt{\mu_{\mathrm{mb}}} = 3.1$ (in black) with respect to $\ln(k_F a_{2\mathrm{D}})$. Here we show the experimental data from Ref. [6]. The experimental critical temperature T_c/T_F with the corresponding statistical errors is depicted in white, while the color scale denotes the nonthermal fraction which signals the onset of a presuperfluid phase.

gas in reduced dimensionality. Here, for small confinement length scales, a substantial reduction of the critical temperature T_c/T_F on the one hand is found on the BEC side of the crossover, while on the other hand the critical temperature on the BCS side is moderately increased. Notably, in the strongly coupled regime, a substantially higher critical temperature is found which is on par with recent measurements [6].

Within the dimensional crossover from three to two dimensions, a diplike structure with regions of increased and reduced critical temperature T_c/T_F were found. This diplike structure is more or less pronounced depending on the scattering length chosen in the ultraviolet $a_{3\mathrm{D}}$ and its exact shape is an artifact of the boundary conditions chosen for the confinement. For a harmonic confinement, similar dips were seen in Ref. [27] for a mean-field study of the critical temperature on the BCS side for quasi-two-dimensional Fermi gases. Moreover, in confined superconducting systems this behavior is known as superconducting shape resonances and responsible for an increased critical temperature, gap, and intrapair correlation length at the discontinuities of the density of states.

These results suggest that a geometry lying between three and two dimensions might be beneficial in finding systems with increased critical temperature and thus in advancing in the quest for high-T_c superconductors.

Overall, we see that certain effects can be attributed to the dimensionality of the system. These include the diplike structure of increased and reduced critical temperature within the dimensional crossover or the overall shape of the phase diagram at a certain confinement length $L\sqrt{\mu_{\mathrm{mb}}}$. The effective dimension of the system has thus a constraining impact on the many-body physics.

The above procedure of confinement from three to two dimensions can in general be extended to confinements from three to one and from two to one dimensions; cf., e.g., Ref. [100] for a dimensional crossover from two to one dimensions. Moreover, for a more realistic confinement scenario, a harmonic trapping potential $V(z) = \frac{1}{2}m\omega_z z^2$, as it is approximately realized in most ultracold atom experiments, should

be implemented instead of the periodic conditions used in this work in order to account for the correct trapping geometry. However, already the periodic boundary conditions yield qualitatively similar features in the L dependence of the critical temperature as a harmonic trap.

A further quantitative improvement, within the dimensional crossover as well as in three dimensions, concerns the calculation of the density by which every quantity is normalized, by means of the Fermi momentum k_F. As detailed in Appendix B, the initial conditions for observables g_i with scaling dimension $d_{g_i} \geqslant 2$ are dependent on the chemical potential μ. As a consequence, the flow of the density, calculated by an μ derivative of the effective potential, is not UV finite. In Appendix B, we outline an iterative safe way of calculating the density whose results will be presented in future work. In addition, the truncation may be extended to include also the renormalization of the fermion propagator, as well as higher orders in the derivative expansion.

Another interesting aspect would be the study of spin- and mass-imbalanced Fermi gases within the dimensional crossover, since here the influence of mismatching Fermi surfaces and stronger fluctuations in lower dimensions might result in competing effects concerning pairing [101–106]. This may shed further physical insight, for example, into the search for high-temperature superconductors.

Already at the present stage our beyond-mean-field analysis is an advancement in the study of the interplay between many-body physics and dimensionality of ultracold Fermi gases. It reveals that the dependence of fluctuation effects on the effective dimensionality leads to characteristic features that can be exploited in experiment and serve as a test for theoretical methods.

APPENDIX A: DEPENDENCE ON THE IR RG-FLOW SCALE

As mentioned in Sec. II D, the running of the couplings does not saturate as quickly in $d < 3$ as in three dimensions in our RG flow. In Fig. 10, we show this IR-scale dependence exemplary for a confinement length of $L\sqrt{\mu_{mb}} = 0.7$ and find that it is most pronounced in the strongly interacting region around $\ln(k_F a_{2\mathrm{D}}) \approx 1$ while being much less significant in the BEC and BCS limits. Seeing that the critical temperature is reduced for a smaller IR scale demands that we choose a sufficiently small final k scale when solving our flow equations.

The dependence on the final RG-flow scale in the infrared across the dimensional crossover can be seen in Fig. 11 for
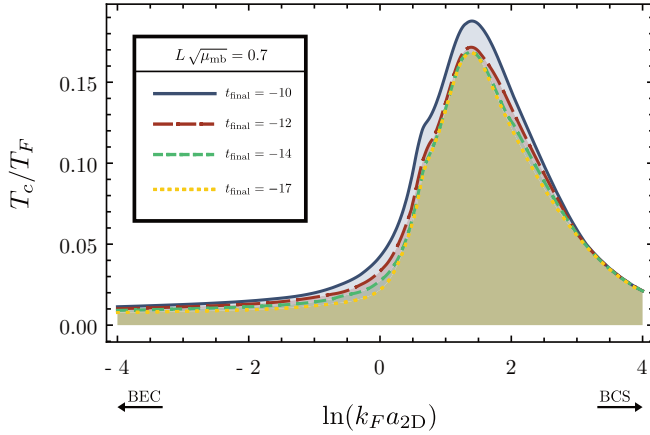
FIG. 10. Phase diagram in terms of T_c/T_F for a confinement length of $L\sqrt{\mu_{mb}} = 0.7$. Here the dependence on the final IR scale of the RG flow is shown with (from top to bottom) $t_{final} = -10$ in solid blue (solid line dark gray), $t_{final} = -12$ in long-dashed red (long-dashed line in gray), $t_{final} = -14$ in dashed green (dashed line in lighter gray), and $t_{final} = -17$ in dotted yellow (dotted line in light gray). It is most pronounced in the strongly interacting region around $\ln k_F a_{2D} \approx 1$, while being much less significant in the BEC and BCS limits. A smaller IR scale leads to a reduced critical temperature.

a three-dimensional scattering length of $a_{3D}^{-1} = 0$. Again, the dips within the crossover from two to three dimensions are caused by the chosen boundary conditions and are related to the steplike structure of the density of states for a confined system [27].

As shown in Fig. 12, the maximum critical temperature T_c^{max}/T_F within the (quasi-)two-dimensional BCS-BEC crossover for a confinement length scale $L\sqrt{\mu_{mb}} = 0.7$ converges for $t_{final} \leqslant -16$. For this reason, we choose a final IR scale of $t_{final} = -17$ for all our calculations such that sufficiently converged results should be obtained.
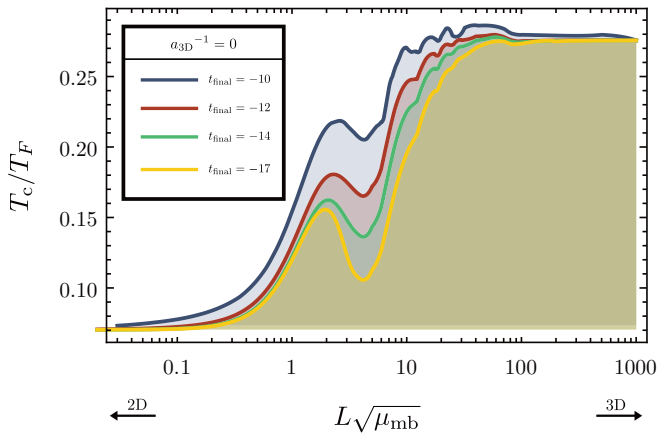

FIG. 11. Critical temperature T_c/T_F at fixed three-dimensional scattering length $a_{3D}^{-1} = 0$ over the dimensional crossover from two to three dimensions. Here we show the dependence on the final IR scale of the RG flow with (from top to bottom) $t_{final} = -10$ in blue (dark gray), $t_{final} = -12$ in red (gray), $t_{final} = -14$ in green (lighter gray), and $t_{final} = -17$ in yellow (light gray).
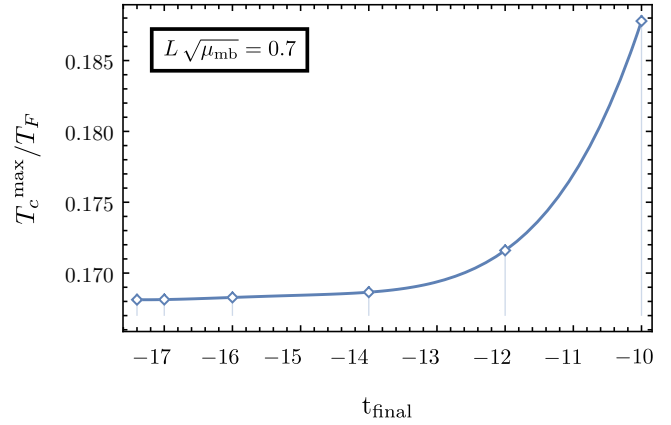

FIG. 12. Maximum critical temperature T_c^{max}/T_F within the (quasi-)two-dimensional BCS-BEC crossover for a confinement length scale $L\sqrt{\mu_{mb}}$ and different final k scales in the infrared. The convergence for $t_{final} \leqslant -16$ can be inferred.

APPENDIX B: μ DEPENDENCE

In this Appendix, we discuss the potential μ dependences of initial conditions as well as an iterative safe way of how to extract related observables such as the density and higher μ derivatives of the free energy. A similar procedure can be found in Ref. [107].

It is well known that thermal fluctuations decay exponentially with the infrared cutoff scale,

$$f(k/T, R)e^{-c(R)k/T}, \tag{B1}$$

where $f(k/T, R)$ rises not more than polynomially or even decays, depending on the (canonical) dimension of the observable under consideration; see Ref. [108]. The form of the prefactor as well as the coefficient $c(R)$ depend on the shape of the regulator. In particular, for nonanalytic cutoffs (in frequency) such as the sharp cutoff and the optimal cutoff, we have $c(R) = 0$ and the thermal behavior at large cutoff scales relates to the dimension of the observable. Note that (B1) can be shown to hold to any order of a given approximation scheme and hence is a formal, exact property of thermal fluctuations. It is intimately linked to the fact that thermal sums can be represented as contour integrals and the infrared cutoff scale serves as a mass parameter which shifts poles to momenta $p^2 \propto ik^2$. This also hints at the fact that it is not present for nonanalytic regulators, where the Matsubara sum cannot be represented as a contour integral and a naive dimensional analysis prevails.

In contradistinction, the chemical potential μ as well as other external tuning parameters only lead to a polynomial decay or rise in the dimensionless ratio

$$\hat{k} = \frac{k}{\mu}, \quad \hat{k} = \frac{k}{\sqrt{\mu}}, \tag{B2}$$

for the relativistic case and nonrelativistic case respectively. In most cases, this behavior is related to the (canonical) dimension of the observable at hand. For example, the free energy or effective action has a vanishing canonical dimension. However, it relates to (negative) pressure times space-time volume $\mathcal{V}$ and hence has a scaling dimension $d_p =$

d with the cutoff scales in the relativistic case and scaling dimension $d_p = d + 1$ in the nonrelativistic case.

The above arguments entail that the flow of the thermal pressure,

$$\partial_t p(T, \mu) := -\left(\frac{\partial_t \Gamma_k[\phi_{\text{EoS},k}; T, \mu]}{\mathcal{V}_T} - \frac{\partial_t \Gamma_k[\phi_{\text{EoS},k}; 0, \mu]}{\mathcal{V}_0} \right), \tag{B3}$$

in general decays exponentially for large cutoff scales,

$$\partial_t p(T, \mu) \propto e^{-c(R)k/T}, \tag{B4}$$

while the free energy density, f, normalized in the vacuum,

$$\partial_t f(T, \mu) := \left(\frac{\partial_t \Gamma_k[\phi_{\text{EoS},k}; T, \mu]}{\mathcal{V}_T} - \frac{\partial_t \Gamma_k[\phi_{\text{EoS},k}; 0, 0]}{\mathcal{V}_0} \right), \tag{B5}$$

has polynomial growth with k,

$$\partial_t f(T, \mu) \to c_{d_f-2} k^{d_f} \hat{k}^{-2} + c_{d_f-4} k^{d_f} \hat{k}^{-4} + k^{d_f} O(\hat{k}^{-6}), \tag{B6}$$

Here, vanishing exponents (in the relativistic case) include logarithms.

1. Initial conditions

Evidently, the initial conditions for observables or couplings g_i with scaling dimension $d_{g_i} \geqslant 2$ are μ dependent. In turn, for sufficiently large cutoff scales $\hat{k} \gg 1$, the initial conditions for couplings with scaling dimension $d_{g_i} < 2$ do not change when changing the chemical potential.

First we concentrate on the effective action, the flow of which is the master equation in our approach,

$$\partial_t \Gamma_k[\psi, \phi] = \frac{1}{2} \text{Tr} \, G_{k,\phi} \, \partial_t R_{k,\phi} - \text{Tr} \, G_{k,\psi} \, \partial_t R_{k,\psi}, \tag{B7}$$

where the field ϕ stands for bosonic fields while ψ stands for fermionic ones. Every observable and coupling can be derived directly from (B7) and its solution. Indeed, if different definitions of observables such as the density exist, the one *directly* using the flow (B7) has the smallest systematic uncertainty.

For our investigation, we write the effective action as

$$\Gamma_k = \Gamma_k[\psi, \phi; \vec{g}], \quad \vec{g} = (m_\psi, m_\phi, Z_\psi, Z_\phi, h, \lambda_\psi, \lambda_\phi, \ldots), \tag{B8}$$

where $\vec{g}$ encodes all couplings (expansion coefficients) of the effective action, ordered in decaying mass dimension. We conclude that in $d = 4$ dimensions the only couplings that potentially require μ-dependent initial conditions are the mass parameters (including μ itself). However, the flow of the dimer mass reads asymptotically

$$\partial_t m_\phi^2 \propto k \frac{h^2}{k} (1 + \mu/k^2)^{3/2} \tag{B9}$$

and hence its μ derivative tends toward zero, and the only coupling to be taken care of is the fermionic mass (and chemical potential).

2. Density

As already mentioned above, the equation for the density with the smallest systematic error is its flow. For the nonrela-

tivistic case, it reads

$$\partial_t n = \frac{1}{\text{Vol}} \frac{d \partial_t \Gamma_k}{d \mu} \to c_{n,3} k^3 + c_{n,1} \mu \, k + O(\hat{k}^{-1}), \tag{B10}$$

and a similar equation holds for the relativistic case. The flow of the susceptibility reads

$$\partial_t \partial_\mu n = \frac{1}{\text{Vol}} \frac{d^2 \partial_t \Gamma_k}{d \mu^2} \to c_{n,1} k + O(\hat{k}^{-1}), \tag{B11}$$

while the flow of the second μ derivative of the density tends toward zero for large cutoff scales,

$$\partial_t \partial_\mu^2 n = \frac{\partial_\mu^3 \partial_t \Gamma_k}{\text{Vol}} \to O(\hat{k}^{-1}). \tag{B12}$$

We conclude that we can represent the density and the susceptibility at vanishing cutoff, $k = 0$, by

$$n(\mu) = \int_0^\mu d\mu' \partial_{\mu'} n(\mu'), \quad \text{with} \quad n(0) = 0, \tag{B13}$$

and

$$\partial_\mu n(\mu) = \int_0^\mu d\mu' \, \partial_{\mu'}^2 n(\mu'), \quad \text{with} \quad \partial_\mu n(0) = 0. \tag{B14}$$

It is left to determine $\partial_\mu^2 n_k(\mu)$. To that end, we rewrite the flow of the density as

$$\partial_t n_k = \frac{d \partial_t \Gamma_k}{d \mu} = \partial_\mu|_{\vec{g}} \partial_t \Gamma_k + \frac{d g_i}{d \mu} \partial_{g_i} \partial_t \Gamma_k. \tag{B15}$$

Both terms follows analytically from the master equation, (B7), and each partial μ derivative and $d g_i / d \mu \, \partial_{g_i}$ derivative lowers the effective k dimension by two. The coefficients $g_i^{(1)} = d g_i / d \mu$ with

$$g_i^{(n)} = \frac{d^n g_i}{d \mu^n} \tag{B16}$$

follow from their flow

$$\partial_t g_i^{(1)} = \frac{d}{d \mu} \partial_t g_i = \partial_\mu \partial_t g_i + g_j^{(1)} \partial_{g_j} \partial_t g_i. \tag{B17}$$

Equation (B17) is a coupled differential equation for $\vec{g}^{(1)}$,

$$\partial_t \vec{g}^{(1)} = \vec{A}_1 + B_1 \cdot \vec{g}^{(1)} \tag{B18}$$

with coefficients

$$A_{1,i} = \partial_\mu \partial_t g_i, \quad B_{1,ij} = \partial_{g_j} \partial_t g_i. \tag{B19}$$

The coefficients $A_{1,i}$ and $B_{1,ij}$ can be read off from the flow (B7), and hence (B18) is a so-called derived flow: It does not feed back into the flow of the effective action. Naturally, this can be iteratively extended to the higher derivatives with regard to μ. For $g_i^{(2)}$, it reads

$$\partial_t g_i^{(2)} = \frac{d}{d \mu} \left(A_{1,i} + B_{1,ij} g_j^{(1)} \right)$$

$$= \partial_\mu A_{1,i} + g_j^{(1)} \partial_{g_j} A_{1,i} + g_j^{(1)} \left(\partial_\mu + g_m^{(1)} \partial_{g_m} \right) B_{1,ij}$$

$$+ B_{1,ij} g_j^{(2)}. \tag{B20}$$

Again, this can be conveniently rewritten in terms of a system of linear differential equations

$$\partial_t \vec{g}^{(2)} = \vec{A}_2 + B_2 \vec{g}^{(2)}, \tag{B21}$$

with

$$A_{2,i} = \left(\partial_\mu + g_m^{(1)} \partial_{g_m}\right) A_{1,i} + g_j^{(1)} \left(\partial_\mu + g_m^{(1)} \partial_{g_m}\right) B_{1,ij},$$
$$B_{2,ij} = B_{1,ij}. \tag{B22}$$

More explicitly, we have

$$A_{2,i} = \partial_\mu^2 \partial_t g_i + 2 g_j^{(1)} \partial_{g_j} \partial_\mu \partial_t g_i + g_j^{(1)} g_m^{(1)} \partial_{g_m} \partial_{g_j} \partial_t g_i,$$
$$B_{2,ij} = \partial_{g_j} \partial_t g_i. \tag{B23}$$

This already allows us to put down the general structure. At a given order $g_i^{(n)}$, the matrix B_n is simply B_1. The vector A_n depends on $\vec{g}, \vec{g}^{(1)}, ..., \vec{g}^{(n-1)}$. Hence, it can be determined iteratively with

$$A_{n,i} = \left(\partial_\mu + \sum_{m=1}^{n-1} g_j^{(m)} \partial_{g_j^{(m-1)}}\right) A_{n-1,i} + g_j^{(n-1)}\left(\partial_\mu + g_m^{(1)} \partial_{g_m}\right) B_{ij} \tag{B24}$$

with $g_i^{(0)} = g_i$ and

$$\left(\partial_\mu + g_m^{(1)} \partial_{g_m}\right) B_{ij} = \partial_\mu \partial_{g_j} \partial_t g_i + g_m^{(1)} \partial_{g_m} \partial_{g_j} \partial_t g_i. \tag{B25}$$

For $n = 3$, this explicitly yields

$$A_{3,i} = \left[\partial_\mu^3 + 3 g_j^{(1)} \partial_{g_j} \partial_\mu^2 + 3 g_j^{(1)} g_m^{(1)} \partial_{g_m} \partial_{g_j} \partial_\mu \right.$$
$$+ g_k^{(1)} g_j^{(1)} g_m^{(1)} \partial_{g_m} \partial_{g_j} \partial_{g_k} + 3 g_m^{(2)} \partial_{g_m} \partial_\mu$$
$$\left. + 3 g_j^{(2)} g_m^{(1)} \partial_{g_m} \partial_{g_j}\right] \partial_t g_i. \tag{B26}$$

Note that there are various forms for the coefficients A_n and B_n. The above forms have the advantage that all derivatives with regard to μ and $g_i^{(n)}$ can be performed analytically. Finally, we write down the flow for higher μ derivatives of Γ_k

$$\partial_\mu^{(n-1)} \dot{n}(\mu) = \frac{d^n \partial_t \Gamma}{d\mu^n} = \left(\partial_\mu + \sum_{m=1}^n g_j^{(m)} \partial_{g_j^{(m-1)}}\right) C_{n-1}, \tag{B27}$$

with

$$C_0 = \partial_t \Gamma_k. \tag{B28}$$

For $n = 2$, this explicitly yields

$$\partial_\mu \partial_t n_k = \frac{d^2 \partial_t \Gamma_k}{d\mu^2} = \left[\partial_\mu^2\big|_{\vec{g}} + 2 g_i^{(1)} \partial_{g_i} \partial_\mu \right.$$
$$\left. + g_j^{(1)} g_i^{(1)} \partial_{g_i} \partial_{g_j} + g_i^{(2)} \partial_{g_i}\right] \partial_t \Gamma_k, \tag{B29}$$

while the second μ derivative of the flow for the density is found to be

$$\partial_\mu^2 \partial_t n_k = \frac{d^3 \partial_t \Gamma_k}{d\mu^3}$$
$$= \left[\partial_\mu^3\big|_{\vec{g}} + 3 g_i^{(1)} \partial_{g_i} \partial_\mu^2 + 3 g_j^{(1)} g_i^{(1)} \partial_{g_i} \partial_{g_j} \partial_\mu\right.$$
$$+ g_m^{(1)} g_j^{(1)} g_i^{(1)} \partial_{g_i} \partial_{g_j} \partial_{g_m} + 3 g_i^{(2)} \partial_{g_i} \partial_\mu$$
$$\left. + 3 g_i^{(2)} g_j^{(1)} \partial_{g_j} \partial_{g_i} + g_i^{(3)} \partial_{g_i}\right] \partial_t \Gamma_k.$$

Hence, overall the density at vanishing cutoff $k = 0$ is obtained by integrating twice over the chemical potential

$$n(\mu) = \int_0^\mu d\mu' \left[\int_0^{\mu'} d\mu'' \partial_{\mu''}^2 n(\mu'') + \partial_{\mu'} n(0)\right] + n(0), \tag{B30}$$

where $n(0)$ and $\partial_\mu n(0)$ are vanishing.

Moreover, we have

$$\partial_\mu^2 n_{k=0}(\mu) = \int_\Lambda^0 \frac{dk}{k} \partial_\mu^2 \dot{n}_k(\mu) \tag{B31}$$

for a UV vanishing flow $\partial_\mu^2 \dot{n}_{k\to\infty} \to 0$.

APPENDIX C: FLOW EQUATIONS

In this Appendix, we derive the flow equations for an ultracold Fermi gas in the dimensional crossover. By defining a master equation, all flow equations of the individual couplings can be obtained by suitable projection descriptions. Furthermore, we consider only the isotropic case where the flow of the couplings in transversal direction equal the ones in the plane $g_i = g_{i,z}$, since this distinction is negligible [75]. Our procedure is based on Ref. [67].

The ansatz for the effective average action can be divided in an kinetic part which consists of the fermion and boson dynamics and interaction part

$$\Gamma_k = \Gamma_{\text{kin}} + \Gamma_{\text{int}}. \tag{C1}$$

The kinetic part in terms of the renormalized fields $\psi = A_\psi^{1/2} \overline{\psi}$ and $\phi = A_\phi^{1/2} \overline{\phi}$ is given by

$$\Gamma_{\text{kin}}[\psi, \phi] = \int_X \left[\sum_{\sigma=\{1,2\}} \psi_\sigma^* (S_\psi \partial_\tau - \nabla^2 + m_\psi) \psi_\sigma \right.$$
$$\left. + \phi^* (S_\phi \partial_\tau - V_\phi \partial_\tau^2 - \nabla^2/2) \phi\right]. \tag{C2}$$

In this work, we set $V_\phi = 0$. We normalized the coefficients of the gradient terms by means of the wave function renormalizations A_ψ and A_ϕ which enter the renormalization group flow via the anomalous dimensions

$$\eta_\psi = -\partial_t \ln A_\psi, \quad \eta_\phi = -\partial_t \ln A_\phi. \tag{C3}$$

Unrenormalized quantities are in the following denoted with an overbar, while renormalized ones do not have overbars. The effective action $\overline{\Gamma}[\overline{\psi}, \overline{\phi}]$ is expressed in terms of the unrenormalized fields. It can, however, be rescaled by appropriate powers of $A_{\psi,\phi}$ such that $\overline{\Gamma}[\overline{\psi}, \overline{\phi}] = \Gamma[\psi, \phi]$. The projection description is performed for the unrenomalized quantities, but the flow is evaluated for the renormalized ones. The interactions can, after a Hubbard-Stratonovich transformation, be written as

$$\Gamma_{\text{int}}[\psi, \phi] = \int_X (U(\phi^* \phi) - h(\phi^* \psi_1 \psi_2 - \phi \psi_1^* \psi_2^*)), \tag{C4}$$

neglecting the RG flow of the four-fermion vertex $\lambda_{\psi,k}$.

The effective average potential depends only on the U(1)-invariant quantity $\rho = \phi^* \phi$ and describes bosonic scattering

processes. The U(1) symmetry is spontaneously broken for a nonzero minimum ρ_0 of the effective average potential and thus describes superfluidity.

In a Taylor expansion, we write

$$U(\rho) = m_\phi^2 (\rho - \rho_0) + \frac{\lambda_\phi}{2}(\rho - \rho_0)^2$$
$$- n_k \, \delta\mu + \alpha_k \, (\rho - \rho_0) \, \delta\mu, \qquad (C5)$$

where we need to include at least up to the second order in ρ to reproduce the second-order phase transition to superfluidity. In the symmetric regime, we therefore have $\rho_0 = 0$ and $m_\phi^2 > 0$, whereas the symmetry-broken regime is realized for $\rho_0 > 0$ and $m_\phi^2 = 0$.

1. Truncation

By including only the fermionic diagrams (F) of Fig. 1, we arrive at the mean-field result and the bosonic fluctuations are taken care of by the diagrams including two bosonic lines (B).

The inverse propagators $\overline{G}_\phi^{-1}(Q)$ and $\overline{G}_\psi^{-1}(Q)$ are calculated by

$$\overline{\Gamma}^{(2)}_{\overline{\phi}_i, \overline{\phi}_j}(X, Y, \overline{\rho}) = \frac{\delta^2 \, \overline{\Gamma}}{\delta \overline{\phi}_i(X) \, \delta \overline{\phi}_j(Y)}[\overline{\phi}],$$

$$\overline{\Gamma}^{(2)}_{\overline{\psi}_\alpha^{(*)}, \overline{\psi}_\beta^{(*)}}(X, Y, \overline{\rho}) = \frac{\overrightarrow{\delta}}{\delta \overline{\psi}_\alpha^{(*)}(X)} \, \overline{\Gamma} \, \frac{\overleftarrow{\delta}}{\delta \overline{\psi}_\beta^{(*)}(Y)}[\overline{\phi}],$$

$$(C6)$$

where the boson background field ϕ is assumed to be real valued and the direction of the arrow for the inverse fermion propagator denotes derivatives acting from left and right on the effective potential. In momentum space, we arrive at

$$\overline{\Gamma}^{(2)}_{BB}(Q, Q') = \delta(Q + Q') \overline{G}_\phi^{-1}(Q),$$
$$\overline{\Gamma}^{(2)}_{FF}(Q, Q') = \delta(Q + Q') \overline{G}_\psi^{-1}(Q). \qquad (C7)$$

After performing the functional derivatives, we obtain in the $\{\phi_1, \phi_2\}$ basis for a constant bosonic background field $\phi = \sqrt{\rho}$

$$\overline{G}_\phi^{-1}(Q) = A_\phi \begin{pmatrix} P_\phi^{S,Q} + U' + 2\,\rho\,U'' & i\,P_\phi^{A,Q} \\ -i\,P_\phi^{A,Q} & P_\phi^{S,Q} + U' \end{pmatrix},$$

$$\overline{G}_\psi^{-1}(Q) = A_\psi \begin{pmatrix} -h\sqrt{\rho}\,\epsilon & -P_\psi^{-Q}\,\mathbb{1} \\ P_\psi^Q\,\mathbb{1} & h\sqrt{\rho}\,\epsilon \end{pmatrix}, \qquad (C8)$$

with $= \overline{G}_\Psi^{-1} = A_\phi \, G_\Psi^{-1}(Q)$, $\mathbb{1}$ being the two-dimensional unity matrix, $\epsilon = ((0, 1), (-1, 0))$ the fully antisymmetric tensor, and a prime denotes a derivative with respect to ρ.

The regulators in the $\{\phi_1, \phi_2\}$ basis are given by

$$\overline{R}_\phi^Q = A_\phi \, R_\phi^Q = A_\phi \begin{pmatrix} R_\phi^S(Q) & i\,R_\phi^A(Q) \\ -i\,R_\phi^A(Q) & R_\phi^S(Q) \end{pmatrix},$$

$$\overline{R}_\psi^Q = A_\psi \, R_\psi^Q = A_\psi \begin{pmatrix} 0 & -R_\psi^{-Q}\,\mathbb{1} \\ R_\psi^Q\,\mathbb{1} & 0 \end{pmatrix}. \qquad (C9)$$

Moreover, we defined the symmetrized and antisymmetrized components of the propagators and regulator functions as

$$f^{S,A}(Q) = \frac{f(Q) \pm f(-Q)}{2}. \qquad (C10)$$

By introducing short-hand notations for the sum of propagator and regulator, as well as the determinants

$$L_\psi^Q = P_\psi^Q + R_\psi^Q,$$

$$\det_F^Q = L_\psi^Q \, L_\psi^{-Q} + h^2 \, \rho,$$

$$L_\phi^Q = P_\phi^Q + R_\phi^Q + U' + \rho\,U'', \qquad (C11)$$

$$\tilde{L}_\phi^Q = P_\phi^Q + R_\phi^Q,$$

$$\det_B^Q = L_\phi^Q \, L_\phi^{-Q} - (\rho U'')^2,$$

we may write the regularized propagators as

$$G_\phi^Q = A_\phi \, \overline{G}_\phi^Q = \frac{1}{\det_B^Q} \begin{pmatrix} \tilde{L}_\phi^{S,Q} + U' & -i\,\tilde{L}_\phi^{A,Q} \\ i\,\tilde{L}_\phi^{A,Q} & \tilde{L}_\phi^{S,Q} + U' + 2\,\rho\,U'' \end{pmatrix},$$

$$G_\psi^Q = A_\psi \, \overline{G}_\psi^Q = \frac{1}{\det_F^Q} \begin{pmatrix} (h^2\,\rho)^{1/2}\,\epsilon & L_\psi^{-Q}\,\mathbb{1} \\ -L_\psi^Q\,\mathbb{1} & -(h^2\,\rho)^{1/2}\,\epsilon \end{pmatrix}. \qquad (C12)$$

We can also represent the boson propagator in the conjugate field basis $\{\phi, \phi^*\}$ where the corresponding matrix will be labeled by a hat.

For $\phi = (\phi_1 + i\,\phi_2)/\sqrt{2}$, we have

$$\begin{pmatrix} \phi \\ \phi^* \end{pmatrix} = \frac{1}{\sqrt{2}} \begin{pmatrix} 1 & i \\ 1 & -i \end{pmatrix} \begin{pmatrix} \phi_1 \\ \phi_2 \end{pmatrix} \qquad (C13)$$

and thus arrive at

$$\widehat{G}_\phi^{-1} = U \, G_\phi^{-1} \, U^t \qquad (C14)$$

with the definitions

$$U = \frac{1}{\sqrt{2}} \begin{pmatrix} 1 & -i \\ 1 & i \end{pmatrix}, \quad U^t = \frac{1}{\sqrt{2}} \begin{pmatrix} 1 & 1 \\ -i & i \end{pmatrix}. \qquad (C15)$$

Thus, we obtain for the inverse boson propagator in the $\{\phi, \phi^*\}$ basis

$$\widehat{G}_\phi^{-1} = \begin{pmatrix} \rho\,U'' & L_\phi^{-Q} \\ L_\phi^Q & \rho\,U'' \end{pmatrix}, \quad \widehat{R}_\phi(Q) = \begin{pmatrix} 0 & R_\phi^{-Q} \\ R_\phi^Q & 0 \end{pmatrix}, \qquad (C16)$$

and

$$\widehat{G}_\phi^Q = \frac{1}{\det_B^Q} \begin{pmatrix} -\rho\,U'' & L_\phi^{-Q} \\ L_\phi^Q & -\rho\,U'' \end{pmatrix} \qquad (C17)$$

To generate higher n-point functions, further functional derivatives have to be applied, once again paying attention to the correct ordering for fermionic derivatives.

Since we assume momentum- and frequency-independent vertices to close our set of equations, the complexity of the system of differential equations is drastically reduced:

$$\overline{\Gamma}_k^{(n>2)}(Q_1, \ldots, Q_n) = \overline{\gamma}_k^{(n)} \, \delta(Q_1, \ldots, Q_n). \qquad (C18)$$

2. Master equations

In order to solve the Wetterich equation in practice, we need to convert it into a set of coupled differential equations of the correlation functions. We therefore start from a few master equations, namely for the inverse fermion and boson propagators, the effective average potential, and the Feshbach coupling.

In the next step, these equation are projected appropriately to arrive at flow equations for the running couplings $\{g_k\}$.

For general regulators, the flow equation of the effective average potential is then given by

$$
\dot{\overline{U}}_k(\overline{\rho}) = \frac{1}{2}\mathrm{Tr}\int_Q \overline{G}_\phi^Q \dot{\overline{R}}_\phi^{-Q} - \frac{1}{2}\mathrm{Tr}\int_Q \overline{G}_\psi^Q \dot{\overline{R}}_\psi^Q
$$

$$
= \frac{1}{2}\int_Q \frac{1}{A_\phi}\frac{L_\phi^Q \dot{\overline{R}}_\phi^{-Q} + L_\phi^{-Q}\dot{\overline{R}}_\phi^Q}{\det_B^Q}
$$

$$
- \frac{1}{2}\int_Q \frac{1}{A_\psi}\frac{L_\psi^Q \dot{\overline{R}}_\psi^{-Q} + L_\psi^{-Q}\dot{\overline{R}}_\psi^Q}{\det_F^Q}. \tag{C19}
$$

Our flow equations can be divided into a bosonic and a fermionic contribution resulting from bosonic (B) and fermionic (F) diagrams, respectively:

$$
\dot{\overline{U}}(\overline{\rho}) = \dot{U}^{(B)} + \dot{U}^{(F)}. \tag{C20}
$$

Including the additional term of the anomalous dimension, we find the flow for the renormalized quantities, e.g.,

$$
\dot{U}(\rho) = \dot{U}^{(B)} + \dot{U}^{(F)} + \eta_\phi \, \rho \, U'(\rho). \tag{C21}
$$

For the flow of the inverse boson propagator in the $\{\phi_1, \phi_2\}$ basis, we find

$$
\dot{\overline{G}}_{\overline{\phi}_i \overline{\phi}_j}^{-1}(P) = \frac{1}{2}\,\mathrm{Tr}\int_Q \overline{G}_\phi(Q)\,\overline{\gamma}_{\overline{\phi}_i BB}^{(3)}\,\overline{G}_\phi(Q+P)\,\overline{\gamma}_{\overline{\phi}_j BB}^{(3)}\,\overline{G}_\phi(Q)\dot{\overline{R}}_\phi(Q)
$$

$$
+ \frac{1}{2}\,\mathrm{Tr}\int_Q \overline{G}_\phi(Q)\,\overline{\gamma}_{\overline{\phi}_j BB}^{(3)}\,\overline{G}_\phi(Q-P)\,\overline{\gamma}_{\overline{\phi}_i BB}^{(3)}\,\overline{G}_\phi(Q)\dot{\overline{R}}_\phi(Q) - \frac{1}{2}\,\mathrm{Tr}\int_Q \overline{G}_\phi(Q)\,\overline{\gamma}_{\overline{\phi}_i \overline{\phi}_j BB}^{(4)}\,\overline{G}_\phi(Q)
$$

$$
- \frac{1}{2}\,\mathrm{Tr}\int_Q \overline{G}_\psi(Q)\,\overline{\gamma}_{\overline{\phi}_i F|F}^{(3)}\,\overline{G}_\psi(Q+P)\,\overline{\gamma}_{\overline{\phi}_j F|F}^{(3)}\,\overline{G}_\psi(Q)\dot{\overline{R}}_\psi(Q)
$$

$$
- \frac{1}{2}\,\mathrm{Tr}\int_Q \overline{G}_\psi(Q)\,\overline{\gamma}_{\overline{\phi}_j F|F}^{(3)}\,\overline{G}_\psi(Q-P)\,\overline{\gamma}_{\overline{\phi}_i F|F}^{(3)}\,\overline{G}_\psi(Q)\dot{\overline{R}}_\psi(Q). \tag{C22}
$$

Likewise, the flow of the inverse fermion propagator is obtained, taking the Grassmannian nature of fermions in account,

$$
\dot{\overline{G}}_{\overline{\psi}_\alpha \overline{\psi}_\beta}^{-1}(P) = \frac{1}{2}\,\mathrm{Tr}\int_Q \overline{G}_\phi(Q)\,\overline{\gamma}_{\overline{\psi}_\alpha B|F}^{(3)}\,\overline{G}_\psi(Q+P)\,\overline{\gamma}_{F|B\overline{\psi}_\beta}^{(3)}\,\overline{G}_\phi(Q)\dot{\overline{R}}_\phi(Q)
$$

$$
- \frac{1}{2}\,\mathrm{Tr}\int_Q \overline{G}_\phi(Q)\,\overline{\gamma}_{BF|\overline{\psi}_\beta}^{(3)}\,\overline{G}_\psi(Q-P)\,\overline{\gamma}_{\overline{\psi}_\alpha|FB}^{(3)}\,\overline{G}_\phi(Q)\dot{\overline{R}}_\phi(Q)
$$

$$
- \frac{1}{2}\,\mathrm{Tr}\int_Q \overline{G}_\psi(Q)\,\overline{\gamma}_{\overline{\psi}_\alpha|FB}^{(3)}\,\overline{G}_\phi(Q+P)\,\overline{\gamma}_{BF|\overline{\psi}_\phi}^{(3)}\,\overline{G}_\psi(Q)\dot{\overline{R}}_\psi(Q)
$$

$$
+ \frac{1}{2}\,\mathrm{Tr}\int_Q \overline{G}_\psi(Q)\,\overline{\gamma}_{F|B\overline{\psi}_\beta}^{(3)}\,\overline{G}_\phi(Q-P)\,\overline{\gamma}_{\overline{\psi}_\alpha B|F}^{(3)}\,\overline{G}_\psi(Q)\dot{\overline{R}}_\psi(Q). \tag{C23}
$$

3. Projection description for the running couplings

In this section, we derive suitable projection descriptions for the flow equations of the running couplings $\{g_k\}$ and expansion coefficients of the effective average potential $U(\rho)$. We use a derivative expansion of the inverse fermion and boson propagators

$$
\overline{P}_{\psi\sigma}(Q) = Z_{\psi\sigma}\, i\, q_0 + A_{\psi\sigma}\, q^2 - \overline{\mu}
$$
$$
= A_{\psi\sigma}(S_{\psi\sigma}\, i\, q_0 + q^2 - \mu),
$$
$$
\overline{P}_\phi(Q) = Z_\phi\, i\, q_0 + A_\phi\, q^2/2
$$
$$
= A_\phi(S_\phi\, i\, q_0 + q^2/2). \tag{C24}
$$

Here we defined $S_{\psi,\phi} = Z_{\psi,\phi}/A_{\psi,\phi}$ and the renormalized chemical potential $\mu = \overline{\mu}/A_{\psi,\sigma}$. Expanding the effective po-

tential in a Taylor series, we can easily project the flow equation (C19) onto the coefficients

$$
U_k(\rho) = m_\phi^2\,(\rho - \rho_0) + \frac{\lambda_\phi}{2}\,(\rho - \rho_0)^2 + \sum_{n>2}^N \frac{u_n}{n!}\,(\rho - \rho_0)^n. \tag{C25}
$$

There are several candidates for projection descriptions for the running couplings which may at a first glance seem equal. However, as the Wetterich equation is an exact equation incorporating all orders of the effective average action, every projection neglects certain higher order couplings and thus results in different flows. We expect though that our truncation includes the most important effects and a precise projection would only yield negligible modifications. The distinction

between different projection descriptions may also be used for an error estimate.

In the symmetric regime of the flow, we have $\dot{\overline{m}}_\phi^2 = \dot{\overline{U}}'(\rho = 0)$, which makes a place for the flow of $\dot{\overline{\rho}}_0 = -\dot{\overline{U}}'(\rho_0)/\overline{\lambda}_\phi$ in the symmetry-broken regime. For the flow of higher expansion coefficients, one finds

$$\dot{\overline{u}}_n = \partial_t\left(\overline{U}^{(n)}(\overline{\rho}_0)\right) = \dot{\overline{U}}^{(n)}(\overline{\rho}_0) + \overline{u}_{n+1}\dot{\overline{\rho}}_0. \tag{C26}$$

We obtain the flow of the renormalized couplings

$$m_\phi^2 = \frac{\overline{m}_\phi^2}{A_\phi}, \quad \rho_0 = A_\phi\,\overline{\rho}_0, \quad u_n = \frac{\overline{u}_n}{A_\phi^n}, \tag{C27}$$

by

$$\dot{m}_\phi^2 = \eta_\phi\,m_\phi^2 + \frac{\dot{\overline{m}}_\phi^2}{A_\phi}, \quad \dot{\rho}_0 = -\eta_\phi\,\rho_0 + A_\phi\,\dot{\overline{\rho}}_0,$$

$$\dot{u}_n = \eta_\phi\,u_n\,n + \frac{\dot{\overline{u}}_n}{A_\phi^n}. \tag{C28}$$

Since we restrict ourselves to purely fermionic and bosonic diagrams, we have no running of the couplings entering the fermionic propagator.

For the couplings associated with the boson propagator, we obtain

$$\dot{Z}_\phi = -\partial_{p_0}\dot{\overline{G}}^{-1}_{\phi_1\phi_2}(P,\rho_0)\big|_{P=0,\rho_0},$$

$$\dot{A}_\phi = 2\,\partial_{p^2}\dot{\overline{G}}^{-1}_{\phi_2\phi_2}(P,\rho_0)\big|_{P=0,\rho_0}, \tag{C29}$$

and for the renormalized quantities with the anomalous dimension $\eta_\phi = -\dot{A}_\phi/A_\phi$

$$\dot{S}_\phi = \eta_\phi\,S_\phi + \frac{\dot{Z}_\phi}{A_\phi}. \tag{C30}$$

$$\dot{S}_\phi^{(B)} = -4\,S_\phi\,\rho\,U''\int_Q\frac{\dot{\overline{R}}_\phi(q^2)}{A_\phi}\left(\frac{U'' + \rho\,U^{(3)}}{\det_B^2(Q)} + \frac{2\,\rho\,U''\left[\rho\,U''(U'' + \rho\,U^{(3)}) - (2\,U'' + \rho\,U^{(3)})L_\phi^S(Q)\right]}{\det_B^3(Q)}\right),$$

$$\eta_\phi^{(B)} = 4\,\rho\,(U'')^2\int_Q\frac{\dot{\overline{R}}_\phi(q^2)}{A_\phi}\left(\frac{1 + 2R_\pi^{(1)} + 4q^2x^2R_\phi^{(2)}}{\det_B^2(Q)} - \frac{2\,q^2x^2(1 + 2R_\pi^{(1)})^2L_\phi^S(Q)}{\det_B^3(Q)}\right). \tag{C32}$$

After performing the Matsubara sums and the momentum integrations, the overall flow equations in our truncation can be cast into the forms

$$\dot{U}^{(F)}(\rho) = -\frac{16\,v_d}{d}\,k^{d+2}\,\ell_F^{(1,1)},$$

$$\dot{U}^{(B)}(\rho) = \frac{8\,v_d\,2^{d/2}}{d}\,k^{d+2}\,\ell_B^{(1,1)}. \tag{C33}$$

The fermionic contributions to the boson propagator are found to be

$$\dot{S}_\phi^{(F)} = -\frac{16\,h^2\,v_d}{d}\,k^{d-4}\left(\ell_F^{(0,2)} - 2\,w_3\,\ell_F^{(0,3)}\right),$$

$$\eta_\phi^{(F)} = \frac{16\,h^2\,v_d}{d}\,k^{d-4}\,\ell_{F,2}^{(0,2)}, \tag{C34}$$

In the flow equations for the running couplings, we neglected a term proportional to $\dot{\overline{\rho}}_0$ which would be generated if one took the RG time derivative after performing the projections.

4. Flow equations using the optimized regulator

In this section, we use the optimized regulator (9) for deriving the flow equations of the running couplings. These equations will be our main starting point in studying the BCS-BEC crossover in dimensions $2 \leqslant d \leqslant 3$. The advantage of the optimized regulator stems from the possibility of analytically performing the Matsubara summations due to a purely spatial cutoff $q^2 = |\vec{q}|^2$.

The procedure may, however, further be simplified by interchanging the order of the derivative projection and the Matsubara summation. We therefore start again from the general form of the flow of the inverse propagators with the trace not being evaluated so that we can expand the inverse propagators $G(Q \pm P)$ in powers of p_0 and p and perform the projections afterward.

For the fermionic contributions, we arrive at the general flow equations with the loop integration still unevaluated:

$$\dot{S}_\phi^{(F)} = -2\,h^2\,S_\psi\int_Q\frac{\dot{\overline{R}}_\psi(q^2)}{A_\psi}\left(\frac{1}{\det_F^2} - \frac{2\,h^2\,\rho}{\det_F^3}\right),$$

$$\eta_\phi^{(F)} = \frac{8\,h^2}{d}\int_Q\frac{\dot{\overline{R}}_\psi(q^2)}{A_\psi}\frac{q^2\,R_\psi(2)}{\det_F^3}. \tag{C31}$$

The expansion for the bosonic contributions results in the flow equations

while the bosonic contributions are given by

$$\dot{S}_\phi^{(B)} = -\frac{32\,S_\phi}{d}\,\rho\,U''\,v_d\,2^{d/2}\,k^{d-4}\big[(U'' + \rho\,U^{(3)})\,\ell_B^{(0,2)}$$

$$+ 2\,(\rho\,U'')^2\,(U'' + \rho\,U^{(3)})\,k^{-4}\,\ell_B^{(0,3)}$$

$$- 2\,\rho\,U''\,(2\,U'' + \rho\,U^{(3)})\,k^{-2}\,\ell_B^{(1,3)}\big],$$

$$\eta_\phi^{(B)} = 8\,\rho\,(U'')^2\,\frac{v_d\,2^{d/2}}{d}\,k^{d-4}\,\ell_{B,2}^{(0,2)}. \tag{C35}$$

Here we used the definitions for fermionic contributions

$$\ell_F^{(n,m)}(\tilde{\mu},\tilde{T},w_3) = \begin{cases}\ell_2(\tilde{\mu})\,\mathcal{F}_m\big(\sqrt{1+w_3}\big) & n\text{ even}\\ \ell_1(\tilde{\mu})\,\mathcal{F}_m\big(\sqrt{1+w_3}\big) & n\text{ odd}\end{cases} \tag{C36}$$

and

$$\ell_{F,2}^{(n,m)}(\tilde{\mu}, \tilde{T}, w_3) = \begin{cases} \ell_3(\tilde{\mu}) \, \mathcal{F}_m\big(\sqrt{1+w_3}\big) & n \text{ even} \\ \ell_1(\tilde{\mu}) \, \mathcal{F}_m\big(\sqrt{1+w_3}\big) & n \text{ odd} \end{cases}, \tag{C37}$$

where we made use of $w_3 = h^2 \rho / k^4$, as well as $w_1 = U'/k^2$ and $w_2 = \rho \, U''/k^2$. For bosonic diagrams, we defined

$$\ell_B^{(n,m)}(\tilde{T}, w_1, w_2) = \frac{1}{S_\phi^{2m}} \left(1 - \frac{\eta_\phi}{d+2}\right) (1 + w_1 + w_2)^n \, \mathcal{B}_m(\sqrt{(1+w_1)(1+w_1+2\,w_2)}/S_\phi) \tag{C38}$$

and

$$\ell_{B,2}^{(0,m)}(\tilde{T}, w_1, w_2) = \frac{1}{S_\phi^{2m}} \, \mathcal{B}_m(\sqrt{(1+w_1)(1+w_1+2\,w_2)}/S_\phi) = \ell_B^{(0,m)}\big|_{\eta_\phi=0}. \tag{C39}$$

$\mathcal{F}_m(z)$ and $\mathcal{B}_m(z)$ label the fermionic and bosonic Matsubara sums of order m, respectively. The functions ℓ_i are defined as

$$\ell_1(x) = \theta(x+1)\,(x+1)^{d/2} - \theta(x-1)\,(x-1)^{d/2},$$
$$\ell_3(x) = \theta(x+1)\,(x+1)^{d/2} + \theta(x-1)\,(x-1)^{d/2}, \quad \text{(C40)}$$
$$\ell_2(x) = \ell_3(x) - 2\,\theta(x)\,x^{d/2},$$

and the d-dimensional volume integral is given by $v_d^{-1} = 2^{d+1} \pi^{d/2} \, \Gamma(d/2)$.

In order to obtain the flow of the density $n = n_{k \to 0}$, we may split the chemical potential into a reference part μ_0 and an offset $\delta\mu$ such that $\mu = \mu_0 + \delta\mu$. We then expand our effective potential (23) with respect to the offset chemical potential $\delta\mu$ according to

$$U_k(\rho) = \sum_{n=1}^{2} \frac{u_n}{n!} (\rho - \rho_0)^n - n_k \, \delta\mu + \alpha_k \, (\rho - \rho_0) \, \delta\mu. \tag{C41}$$

The differentiation with respect to μ acts rather on $\delta\mu$ as the reference chemical potential is fixed:

$$\dot{n}_k = -\frac{\partial \dot{U}}{\partial \, \delta\mu}. \tag{C42}$$

According to our master equation for the effective average potential (C19), we now expand $L_\psi^{S,Q}$ and $\det_{\mathrm{F}}^Q$ in terms of $\delta\mu$ while the fermionic cutoff still regularizes around the Fermi surface, i.e., the reference chemical potential μ_0.

5. Flow equations for finite volume

When confining our system by means of a compactification of one spatial dimension in a dimensional crossover from 3d to 2d with a confinement length scale L. By adopting periodic boundary conditions, we restrict our system to a torus in one spatial direction

$$\psi(L) = \psi(0), \tag{C43}$$

such that we obtain a "spatial Matsubara sum" over discrete momenta $k_n = 2\pi n/L$ with $n \in \mathbb{Z}$. Accompanying this quantization of energy levels, the bosonic and fermionic regulators defined are modified accordingly. For the optimized regulator,

they become

$$R_{\phi,k}(q^2) = \left(k^2 - \frac{q^2 + k_n^2}{2}\right) \theta\left(k^2 - \frac{q^2 + k_n^2}{2}\right),$$
$$R_{\psi,k}(q^2) = k^2 \left[\mathrm{sgn}\big(z + \tilde{k}_n^2\big) - \big(z + \tilde{k}_n^2\big)\right] \theta\big(1 - |z + \tilde{k}_n^2|\big), \tag{C44}$$

where we again used $z = (q^2 - \mu)/k^2$ and $\tilde{k}_n = k_n/k$. Hence, the d-dimensional spatial integration splits up into a sum over the discrete momenta k_n and a momentum integral in $d-1$ dimensions

$$\int \frac{d^d q}{(2\pi)^d} = \frac{1}{L} \sum_{k_n} \int \frac{d^{d-1} q}{(2\pi)^{d-1}}. \tag{C45}$$

Due to the inclusion of the discrete momenta in the regulator, the evaluation of the spatial boils down to counting the modes within the potential well. For periodic boundary conditions, we hereby encounter the following type of sums:

$$\sum_{n=-N}^{N} \alpha = \alpha \, (1 + 2N) \quad (\alpha \in \mathbb{R}),$$
$$\sum_{n=1}^{N} n^2 = \frac{1}{6} N \, (1 + N) \, (1 + 2N), \tag{C46}$$

and

$$\sum_{n=1}^{N} n^4 = \frac{1}{30} N \, (1 + N) \, (1 + 2N) \, (-1 + 3N + 3N^2). \tag{C47}$$

As a result of the periodic boundary conditions, the regulator function restricts the Matsubara-type summation in the transversal direction to $|k_n| = |2\pi n/L| < \sqrt{2}\,k$ or equivalently $|n| < \tilde{L}/\sqrt{2}\pi$.

For bosonic contributions, we define

$$N^{(B)} = \left\lfloor \frac{\tilde{L}}{\sqrt{2}\,\pi} \right\rfloor \tag{C48}$$

with $\lfloor x \rfloor$ being the largest integer smaller than x. In three dimensions, we find

$$
\begin{aligned}
C_L &= \frac{1}{L} \sum_{k_n} \left(1 - \frac{k_n^2}{2\,k^2} \right)^{d/2} \left[1 - \frac{\eta_\phi}{d+2} \left(1 - \frac{k_n^2}{2\,k^2} \right) \right] \theta\left(k^2 - \frac{k_n^2}{2} \right) \\
&= \frac{k}{\tilde{L}} (1 + 2 N^{(B)}) \left\{ 1 - \frac{\eta_\phi}{4} - \frac{1}{6} \left(1 - \frac{\eta\phi}{2} \right) \left(\frac{2\pi}{\tilde{L}} \right)^2 N^{(B)} (1 + N^{(B)}) \right. \\
&\quad \left. - \frac{\eta_\phi}{60} \left(\frac{2\pi}{\tilde{L}} \right)^4 N^{(B)} (1 + N^{(B)}) [-1 + 3 N^{(B)} + 3 (N^{(B)})^2] \right\}.
\end{aligned}
\tag{C49}
$$

Thus, all bosonic flow equations still hold with the replacements

$$
\left(1 - \frac{\eta_\phi}{d+2} \right) \to C_L, \quad d \to d-1.
\tag{C50}
$$

The fermionic momentum integrals can be generalized by the transformation $z \to \hat{z} = (q^2 + k_n^2 - \mu)/k^2$. All results can then be transferred by the transformation $\mu \to \hat{\mu} = \tilde{\mu} - \tilde{k}_n^2$. For periodic boundary conditions, it can be easily shown in $d = 3$ dimensions

$$
\frac{1}{L} \sum_{k_n} \theta(\hat{\mu}+1)(\hat{\mu}+1)^{(d-1)/2} = \frac{1}{L} \left[(\tilde{\mu}+1)(1 + 2 N_1^{(F)}) - \frac{1}{3} \left(\frac{2\pi}{\tilde{L}} \right)^2 N_1^{(F)} (1 + N_1^{(F)}) (1 + 2 N_1^{(F)}) \right] \theta(\tilde{\mu}+1),
$$

$$
\frac{1}{L} \sum_{k_n} \theta(\hat{\mu}-1)(\hat{\mu}-1)^{(d-1)/2} = \frac{1}{L} \left[(\tilde{\mu}-1)(1 + 2 N_2^{(F)}) - \frac{1}{3} \left(\frac{2\pi}{\tilde{L}} \right)^2 N_2^{(F)} (1 + N_2^{(F)}) (1 + 2 N_2^{(F)}) \right] \theta(\tilde{\mu}-1),
$$

$$
\frac{1}{L} \sum_{k_n} \theta(\hat{\mu})(\hat{\mu})^{(d-1)/2} = \frac{1}{L} \left[\tilde{\mu} (1 + 2 N_3^{(F)}) - \frac{1}{3} \left(\frac{2\pi}{\tilde{L}} \right)^2 N_3^{(F)} (1 + N_3^{(F)}) (1 + 2 N_3^{(F)}) \right] \theta(\tilde{\mu}).
\tag{C51}
$$

Here we defined

$$
N_1^{(F)} = \left\lfloor \frac{\tilde{L}(\tilde{\mu}+1)^{1/2}}{2\pi} \right\rfloor, \quad N_2^{(F)} = \left\lfloor \frac{\tilde{L}(\tilde{\mu}-1)^{1/2}}{2\pi} \right\rfloor, \quad N_3^{(F)} = \left\lfloor \frac{\tilde{L}\tilde{\mu}^{1/2}}{2\pi} \right\rfloor.
\tag{C52}
$$

Hence, for the spatial threshold function with explicit Matsubara summation, we obtain for periodic boundary conditions in $d = 3$

$$
\begin{aligned}
\frac{1}{L} \sum_{k_n} \ell_a(\hat{\mu}) &= \frac{k}{\tilde{L}} \left\{ \left[(\tilde{\mu}+1)(1 + 2 N_1^{(F)}) - \frac{1}{3} \left(\frac{2\pi}{\tilde{L}} \right)^2 N_1^{(F)} (1 + N_1^{(F)}) (1 + 2 N_1^{(F)}) \right] \right. \\
&\quad \times (-1)^a \left[(\tilde{\mu}+1) \to (\tilde{\mu}-1)\left(N_1^{(F)} \to N_2^{(F)} \right) \right] \\
&\quad \left. - (1 + (-1)^a) \left[\tilde{\mu} (1 + 2 N_3^{(F)}) - \frac{1}{3} \left(\frac{2\pi}{\tilde{L}} \right)^2 N_3^{(F)} (1 + N_3^{(F)}) (1 + 2 N_3^{(F)}) \right] \right\}
\end{aligned}
\tag{C53}
$$

for $a = 1, 2$ and in addition

$$
\begin{aligned}
\frac{1}{L} \sum_{k_n} \ell_3(\hat{\mu}) &= \frac{k}{\tilde{L}} \left\{ \left[(\tilde{\mu}+1)(1 + 2 N_1^{(F)}) - \frac{1}{3} \left(\frac{2\pi}{\tilde{L}} \right)^2 N_1^{(F)} (1 + N_1^{(F)}) (1 + 2 N_1^{(F)}) \right] \right. \\
&\quad \left. + \left[(\tilde{\mu}+1) \to (\tilde{\mu}-1) \& \left(N_1^{(F)} \to N_2^{(F)} \right) \right] \right\}.
\end{aligned}
\tag{C54}
$$

Thus, all fermionic flow equations can be transferred to the case of finite volume with periodic boundary conditions with the replacement

$$
\ell_i \to \ell_{i,L} = \frac{k}{\tilde{L}} \sum_{k_n} \ell_i, \quad d \to d-1.
\tag{C55}
$$

APPENDIX D: NUMERICAL PROCEDURE

The set of coupled differential equations for the projected flow equations from Appendix C are numerically evaluated for both zero and finite temperature. However, it is a useful feature of the functional renormalization group that for large scales $k^2 \gg T$ the finite-temperature flow can be approximated by the zero-temperature system [67]. For a practical computation, we choose $k_{\text{switch},T} = 6\pi T$; i.e., we follow the zero-temperature flow until $k_{\text{switch},T}$ where the temperature starts to become an im-

portant scale and we switch to the finite-temperature flow equations.

Likewise, the Fermi gas confined to a trap can be regarded as an unconfined system for large scales $k \gg L^{-1}$. Here we choose $k_{\mathrm{switch},L} = 50/L$, which significantly decreases the runtime of the computation. The agreement of the results with and without splitting the flow in zero and finite temperature, as well as unconfined and confined flow equations was checked numerically.

The critical temperature is determined as the largest temperature for which the gap of the fermion spec-

trum is nonvanishing. Numerically, we use the following algorithm

$$0 < \Delta_{t_{\mathrm{final}}}(T_c, \mu, a, L) < \frac{1}{100} \Delta_{t_{\mathrm{final}}}(T = 0, \mu, a, L). \quad \text{(D1)}$$

Using this algorithm is very efficient, as it accounts for both the large gap on the BEC side and for the smaller gap on the BCS side (especially in the three-dimensional case). It was checked numerically that further limitation to $<1\%$ of the zero-temperature gap yields identical results in $d \leqslant 3$ within the numerical precision.

[1] M. Lewenstein, A. Sanpera, V. Ahufinger, B. Damski, A. Sen, and U. Sen, Adv. Phys. **56**, 243 (2007).

[2] I. Bloch, J. Dalibard, and W. Zwerger, Rev. Mod. Phys. **80**, 885 (2008).

[3] I. Boettcher, L. Bayha, D. Kedar, P. A. Murthy, M. Neidig, M. G. Ries, A. N. Wenz, G. Zürn, S. Jochim, and T. Enss, Phys. Rev. Lett. **116**, 045303 (2016).

[4] U. Toniolo, B. C. Mulkerin, X.-J. Liu, and H. Hu, Phys. Rev. A **97**, 063622 (2018).

[5] S. Tung, G. Lamporesi, D. Lobser, L. Xia, and E. A. Cornell, Phys. Rev. Lett. **105**, 230408 (2010).

[6] M. G. Ries, A. N. Wenz, G. Zürn, L. Bayha, I. Boettcher, D. Kedar, P. A. Murthy, M. Neidig, T. Lompe, and S. Jochim, Phys. Rev. Lett. **114**, 230401 (2015).

[7] K. Fenech, P. Dyke, T. Peppler, M. G. Lingham, S. Hoinka, H. Hu, and C. J. Vale, Phys. Rev. Lett. **116**, 045302 (2016).

[8] B. C. Mulkerin, X.-J. Liu, and H. Hu, Phys. Rev. A **97**, 053612 (2018).

[9] Z. Hadzibabic, P. Krüger, M. Cheneau, B. Battelier, and J. Dalibard, Nature (London) **441**, 1118 (2006).

[10] P. Cladé, C. Ryu, A. Ramanathan, K. Helmerson, and W. D. Phillips, Phys. Rev. Lett. **102**, 170401 (2009).

[11] T. Plisson, B. Allard, M. Holzmann, G. Salomon, A. Aspect, P. Bouyer, and T. Bourdel, Phys. Rev. A **84**, 061606(R) (2011).

[12] R. Desbuquois, L. Chomaz, T. Yefsah, J. Léonard, J. Beugnon, C. Weitenberg, and J. Dalibard, Nat. Phys. **8**, 645 (2012).

[13] R. J. Fletcher, M. Robert-de-Saint-Vincent, J. Man, N. Navon, R. P. Smith, K. G. H. Viebahn, and Z. Hadzibabic, Phys. Rev. Lett. **114**, 255302 (2015).

[14] P. A. Murthy, I. Boettcher, L. Bayha, M. Holzmann, D. Kedar, M. Neidig, M. G. Ries, A. N. Wenz, G. Zürn, and S. Jochim, Phys. Rev. Lett. **115**, 010401 (2015).

[15] L. P. Pitaevskii and A. Rosch, Phys. Rev. A **55**, R853 (1997).

[16] M. Olshanii, H. Perrin, and V. Lorent, Phys. Rev. Lett. **105**, 095302 (2010).

[17] E. Taylor and M. Randeria, Phys. Rev. Lett. **109**, 135301 (2012).

[18] J. Hofmann, Phys. Rev. Lett. **108**, 185303 (2012).

[19] C. Gao and Z. Yu, Phys. Rev. A **86**, 043609 (2012).

[20] C. Chafin and T. Schäfer, Phys. Rev. A **88**, 043636 (2013).

[21] W. Daza, J. E. Drut, C. Lin, and C. Ordóñez, Phys. Rev. A **97**, 033630 (2018).

[22] H. Hu, B. C. Mulkerin, U. Toniolo, L. He, and X.-J. Liu, Phys. Rev. Lett. **122**, 070401 (2019).

[23] M. Holten, L. Bayha, A. C. Klein, P. A. Murthy, P. M. Preiss, and S. Jochim, Phys. Rev. Lett. **121**, 120401 (2018).

[24] T. Peppler, P. Dyke, M. Zamorano, I. Herrera, S. Hoinka, and C. J. Vale, Phys. Rev. Lett. **121**, 120402 (2018).

[25] P. A. Murthy, N. Defenu, L. Bayha, M. Holten, P. M. Preiss, T. Enss, and S. Jochim, Science **365**, 268 (2019).

[26] A. M. Fischer and M. M. Parish, Phys. Rev. A **88**, 023612 (2013).

[27] A. M. Fischer and M. M. Parish, Phys. Rev. B **90**, 214503 (2014).

[28] J. Braun, S. Diehl, and M. M. Scherer, Phys. Rev. A **84**, 063616 (2011).

[29] M. Bauer, M. M. Parish, and T. Enss, Phys. Rev. Lett. **112**, 135302 (2014).

[30] H. Shi, S. Chiesa, and S. Zhang, Phys. Rev. A **92**, 033603 (2015).

[31] F. Marsiglio, P. Pieri, A. Perali, F. Palestini, and G. C. Strinati, Phys. Rev. B **91**, 054509 (2015).

[32] C.-T. Wu, B. M. Anderson, R. Boyack, and K. Levin, Phys. Rev. Lett. **115**, 240401 (2015).

[33] L. He, H. Lü, G. Cao, H. Hu, and X.-J. Liu, Phys. Rev. A **92**, 023620 (2015).

[34] G. Bighin and L. Salasnich, Phys. Rev. B **93**, 014519 (2016).

[35] L. Salasnich and G. Bighin, J. Supercond. Novel Magn. **29**, 3103 (2016).

[36] B. C. Mulkerin, L. He, P. Dyke, C. J. Vale, X.-J. Liu, and H. Hu, Phys. Rev. A **96**, 053608 (2017).

[37] G. Bighin and L. Salasnich, Int. J. Mod. Phys. B **32**, 1840022 (2018).

[38] F. Wu, J. Hu, L. He, X.-J. Liu, and H. Hu, Phys. Rev. A **101**, 043607 (2020).

[39] J. P. Gaebler, J. T. Stewart, T. E. Drake, D. S. Jin, A. Perali, P. Pieri, and G. C. Strinati, Nat. Phys. **6**, 569 (2010).

[40] P. A. Murthy, M. Neidig, R. Klemt, L. Bayha, I. Boettcher, T. Enss, M. Holten, G. Zürn, P. M. Preiss, and S. Jochim, Science **359**, 452 (2018).

[41] S. Tsuchiya, R. Watanabe, and Y. Ohashi, Phys. Rev. A **80**, 033613 (2009).

[42] M. Matsumoto, R. Hanai, D. Inotani, and Y. Ohashi, J. Phys.: Conf. Ser. **969**, 012012 (2018).

[43] A. Richie-Halford, J. E. Drut, and A. Bulgac, Phys. Rev. Lett. **125**, 060403 (2020).

[44] Y. Chen, A. Shanenko, A. Perali, and F. Peeters, J. Phys. Conden. Matter **24**, 185701 (2012).

[45] A. Guidini and A. Perali, Superconductor Sci. Technol. **27**, 124002 (2014).

[46] A. Guidini, L. Flammia, M. V. Milošević, and A. Perali, J. Supercond. Novel Magn. **29**, 711 (2016).

[47] H. Tajima, A. Perali, and P. Pieri, Condens. Matter **5**, 10 (2020).

[48] S. Rinott, K. B. Chashka, A. Ribak, E. D. L. Rienks, A. Taleb-Ibrahimi, P. Le Fevre, F. Bertran, M. Randeria, and A. Kanigel, Sci. Adv. **3** , 1602372 (2017).

[49] J. M. Blatt and C. J. Thompson, Phys. Rev. Lett. **10**, 332 (1963).

[50] C. Thompson and J. Blatt, Phys. Lett. **5**, 6 (1963).

[51] D. Innocenti, N. Poccia, A. Ricci, A. Valletta, S. Caprara, A. Perali, and A. Bianconi, Phys. Rev. B **82**, 184528 (2010).

[52] A. Bianconi, D. Innocenti, A. Valletta, and A. Perali, J. Phys. Conf. Ser. **529**, 012007 (2014).

[53] N. Pinto, S. J. Rezvani, A. Perali, L. Flammia, M. V. Milošević, M. Fretto, C. Cassiago, and N. De Leo, Sci. Rep. **8**, 4710 (2018).

[54] D. Eom, S. Qin, M.-Y. Chou, and C. K. Shih, Phys. Rev. Lett. **96**, 027005 (2006).

[55] A. Perali, A. Bianconi, A. Lanzara, and N. L. Saini, Solid State Commun. **100**, 181 (1996).

[56] S. Diehl and C. Wetterich, Phys. Rev. A **73**, 033615 (2006).

[57] S. Diehl and C. Wetterich, Nucl. Phys. B **770**, 206 (2007).

[58] S. Diehl, H. Gies, J. M. Pawlowski, and C. Wetterich, Phys. Rev. A **76**, 053627 (2007).

[59] S. Diehl, H. Gies, J. M. Pawlowski, and C. Wetterich, Phys. Rev. A **76**, 021602(R) (2007).

[60] S. Floerchinger, M. Scherer, S. Diehl, and C. Wetterich, Phys. Rev. B **78**, 174528 (2008).

[61] S. Floerchinger, R. Schmidt, S. Moroz, and C. Wetterich, Phys. Rev. A **79**, 013603 (2009).

[62] S. Floerchinger, M. M. Scherer, and C. Wetterich, Phys. Rev. A **81**, 063619 (2010).

[63] S. Diehl, S. Floerchinger, H. Gies, J. M. Pawlowski, and C. Wetterich, Ann. Phys. **522**, 615 (2010).

[64] I. Boettcher, J. M. Pawlowski, and S. Diehl, Nucl. Phys. Proc. Suppl. **228**, 63 (2012).

[65] I. Boettcher, S. Diehl, J. M. Pawlowski, and C. Wetterich, Phys. Rev. A **87**, 023606 (2013).

[66] D. Schnoerr, I. Boettcher, J. M. Pawlowski, and C. Wetterich, Ann. Phys. **334**, 83 (2013).

[67] I. Boettcher, J. M. Pawlowski, and C. Wetterich, Phys. Rev. A **89**, 053630 (2014).

[68] I. Boettcher, J. Braun, T. K. Herbst, J. M. Pawlowski, D. Roscher, and C. Wetterich, Phys. Rev. A **91**, 013610 (2015).

[69] D. Roscher, J. Braun, and J. E. Drut, Phys. Rev. A **91**, 053611 (2015).

[70] I. Boettcher, T. K. Herbst, J. M. Pawlowski, N. Strodthoff, L. von Smekal, and C. Wetterich, Phys. Lett. B **742**, 86 (2015).

[71] M. Ku, J. Braun, and A. Schwenk, Phys. Rev. Lett. **102**, 255301 (2009).

[72] J. Braun, B. Klein, and B.-J. Schaefer, Phys. Lett. B **713**, 216 (2012).

[73] J. Braun, Few Body Syst. **53**, 37 (2012).

[74] R.-A. Tripolt, J. Braun, B. Klein, and B.-J. Schaefer, Phys. Rev. D **90**, 054012 (2014).

[75] S. Lammers, I. Boettcher, and C. Wetterich, Phys. Rev. A **93**, 063631 (2016).

[76] N. Dupuis, L. Canet, A. Eichhorn, W. Metzner, J. M. Pawlowski, M. Tissier, and N. Wschebor, Phys. Rep. (2021), doi: 10.1016/j.physrep.2021.01.001.

[77] C. Wetterich, Nucl. Phys. B **352**, 529 (1991).

[78] C. Wetterich, Phys. Lett. B **301**, 90 (1993).

[79] J. M. Pawlowski, Ann. Phys. **322**, 2831 (2007).

[80] B.-J. Schaefer and J. Wambach, Phys. Part. Nucl. **39**, 1025 (2008).

[81] H. Gies, Lect. Notes Phys. **852**, 287 (2012).

[82] B. Delamotte, Lect. Notes Phys. **852**, 49 (2012).

[83] P. Kopietz, L. Bartosch, and F. Schütz, Lect. Notes Phys. **798**, 1 (2010).

[84] W. Metzner, M. Salmhofer, C. Honerkamp, V. Meden, and K. Schonhammer, Rev. Mod. Phys. **84**, 299 (2012).

[85] J. Braun, J. Phys. G **39**, 033001 (2012).

[86] D. F. Litim, Int. J. Mod. Phys. A **16**, 2081 (2001).

[87] D. F. Litim, Phys. Rev. D **64**, 105007 (2001).

[88] C. Wetterich, Phys. Rev. B **77**, 064504 (2008).

[89] N. Tetradis and C. Wetterich, Nucl. Phys. B **398**, 659 (1993).

[90] N. D. Mermin and H. Wagner, Phys. Rev. Lett. **17**, 1133 (1966).

[91] P. C. Hohenberg, Phys. Rev. **158**, 383 (1967).

[92] V. L. Berezinsky, Sov. Phys. JETP **32**, 493 (1971) [Zh. Eksp. Teor. Fiz. **59**, 907 (1971)].

[93] V. L. Berezinsky, Sov. Phys. JETP **34**, 610 (1972) [Zh. Eksp. Teor. Fiz. **61**, 1144 (1972)].

[94] J. M. Kosterlitz and D. J. Thouless, J. Phys. C **6**, 1181 (1973).

[95] J. M. Kosterlitz, J. Phys. C **7**, 1046 (1974).

[96] K. Miyake, Prog. Theor. Phys. **69**, 1794 (1983).

[97] L. P. Gor'kov and T. K. Melik-Barkhudarov, Sov. Phys. JETP **13**, 1018 (1961) [Zh. Eksp. Teor. Fiz. **40**, 1452 (1961)].

[98] D. S. Petrov, M. A. Baranov, and G. V. Shlyapnikov, Phys. Rev. A **67**, 031601(R) (2003).

[99] J. Levinsen and M. M. Parish, Ann. Rev. Cold Atoms Molecules **3**, 1 (2014).

[100] A. A. Shanenko, M. D. Croitoru, A. V. Vagov, V. M. Axt, A. Perali, and F. M. Peeters, Phys. Rev. A **86**, 033612 (2012).

[101] L. He and P. Zhuang, Phys. Rev. A **78**, 033613 (2008).

[102] K. Sun and C. J. Bolech, Phys. Rev. A **85**, 051607(R) (2012).

[103] W. Ong, C. Cheng, I. Arakelyan, and J. E. Thomas, Phys. Rev. Lett. **114**, 110403 (2015).

[104] D. Mitra, P. T. Brown, P. Schauß, S. S. Kondov, and W. S. Bakr, Phys. Rev. Lett. **117**, 093601 (2016).

[105] C.-T. Wu, R. Boyack, and K. Levin, Phys. Rev. A **94**, 033604 (2016).

[106] S. Dutta and E. J. Mueller, Phys. Rev. A **94**, 063627 (2016).

[107] W.-J. Fu and J. M. Pawlowski, Phys. Rev. D **92**, 116006 (2015).

[108] L. Fister and J. M. Pawlowski, arXiv:1112.5440 [hep-ph].